Mon. Not. R. Astron. Soc. **000**, 1–18 (2013) Printed 27 July 2018 (MN LATEX style file v2.2)

Element Abundances at High-redshift: Magellan MIKE Observations of sub-Damped Lyman-α Absorbers at $1.7 < z < 2.4$

Debopam Som[1], Varsha P. Kulkarni[1], Joseph Meiring[2], Donald G. York[3,4], Celine Péroux[5], Pushpa Khare[6], and James T. Lauroesch[7]

[1]*Department of Physics and Astronomy, University of South Carolina, Columbia, SC 29208, USA*
[2]*Department of Astronomy, University of Massachusetts, Amherst, MA 01003, USA*
[3]*Department of Astronomy and Astrophysics, University of Chicago, Chicago, IL 60637, USA*
[4]*Enrico Fermi Institute, University of Chicago, Chicago, IL 60637, USA*
[5]*Aix-Marseille Université, CNRS, LAM(Laboratoire d'Astrophysique de Marseille) UMR 7326, 13388, Marseille, France*
[6]*CSIR Emeritus Scientist, IUCAA, Pune, India*
[7]*Department of Physics and Astronomy, University of Louisville, Louisville, Ky 40292 USA*

Accepted: 2013 July 24, Received: 2013 July 20; in original form: 2012 November 09

ABSTRACT

We present chemical abundance measurements from high-resolution observations of 5 sub-damped Lyman-α absorbers at $1.7 < z < 2.4$ observed with the Magellan Inamori Kyocera Echelle (MIKE) spectrograph on the 6.5-m Magellan II Clay telescope. Lines of Zn II, Mg I, Mg II, Al II, Al III, S II, Si II, Si IV, C II, C II*, C IV, Ni II, Mn II and Fe II were detected and column densities were determined. The metallicity of the absorbing gas, inferred from the nearly undepleted element Zn, is in the range of < -0.95 to $+0.25$ dex for the five absorbers in our sample, with three of the systems being near-solar or super-solar. We also investigate the effect of ionisation on the observed abundances using photoionisation modelling. Combining our data with other sub-DLA and DLA data from the literature, we report the most complete existing determination of the metallicity vs. redshift relation for sub-DLAs and DLAs. We confirm the suggestion from previous investigations that sub-DLAs are, on average, more metal-rich than DLAs and evolve faster. We also discuss relative abundances and abundance ratios in these absorbers. The more metal-rich systems show significant dust depletion levels, as suggested by the ratios [Zn/Cr] and [Zn/Fe]. For the majority of the systems in our sample, the [Mn/Fe] vs. [Zn/H] trend is consistent with that seen previously for lower-redshift sub-DLAs. We also measure the velocity width values for the sub-DLAs in our sample from unsaturated absorption lines of Fe II $\lambda\lambda\lambda$ 2344, 2374, 2600Å, and examine where these systems lie in a plot of metallicity vs. velocity dispersion. Finally, we examine cooling rate vs. H I column density in these sub-DLAs, and compare this with the data from DLAs and the Milky Way ISM. We find that most of the systems in our sample show higher cooling rate values compared to those seen in the DLAs.

Key words: Quasars: absorption lines-ISM: abundances

1 INTRODUCTION

Many open questions remain about the processes of galaxy formation and evolution. Heavy element abundance measurements in galaxies reveal important information about the ongoing processes of star formation and death, and the overall chemical enrichment of these galaxies. Studying the chemical composition of high-redshift galaxies through emission lines often leads to a bias toward the most actively star-forming galaxies. Moreover, it is difficult to determine abundances accurately from emission line indices. Quasar Absorption Line Systems (QSOALS) provide a way to study the interstellar medium (ISM) of high redshift galaxies independent of the morphology and luminosity of galaxies. In addition, absorption lines in QSO spectra allow us to study the diffuse intergalactic medium using UV or X-ray observations of high-ionization species such as N V, O VI, O VIII, etc. (e.g., Simcoe et al. 2002; Fang et al. 2002).

Quasar absorption line systems with strong Lyman-α lines are often divided into two classes: Damped Lyman-α (DLA, log $N_{H\,I} \geqslant 20.3$) and sub-Damped Lyman-α (sub-DLA, $19 \lesssim \log N_{H\,I} < 20.3$, Péroux et al. 2001). DLAs and sub-DLAs contain a major fraction of the neutral gas in the Universe, while the majority of the baryons are thought to lie in the highly ionized and diffuse Lyman-α forest clouds with log $N_{H\,I} \leqslant 14$ in intergalactic space (e.g.,

Petitjean et al. 1993).The DLA and sub-DLA systems are generally believed to be associated directly with galaxies at all redshifts at which they are found. Indeed, several DLA host galaxies have been confirmed through deep imaging and follow-up spectroscopy (e.g., Chen and Lanzetta 2003; Gharanfoli et al. 2007).

A number of chemical elements are detected in DLAs and sub-DLAs, e.g., C, N, O, Mg, Si, S, Ca, Ti, Cr, Mn, Fe, Ni, and Zn. Among these elements, Zn is often adopted as the tracer of gas-phase metallicity as it is relatively undepleted in the Galactic ISM, especially when the fraction of H in molecular form is low, as is the case in most DLAs. Zn also tracks the Fe abundance in Galactic stars (e.g., Nissen et al. 2004), and the lines of Zn II $\lambda\lambda$ 2026,2062 are relatively weak and typically unsaturated. These lines can also be covered with ground-based spectroscopy over a wide range of redshifts, from $0.65 \lesssim z \lesssim 3.5$, which covers a large portion of the history of the universe. Abundances of refractory elements such as Cr and Fe relative to Zn also give us a measure of the amount of dust depletion (York et al. 2006). Abundance ratios such as [Si/Fe], [O/Fe] and [Mn/Fe] shed light on the enrichment from the different types of supernovae, as the α-capture elements Si and O are produced mainly in Type II supernovae while the iron peak elements are produced mainly by Type Ia supernovae.

The majority of previous studies of element abundances have focused on DLAs because of their high gas content (Prochaska & Wolfe 2002; Kulkarni et al. 2005; Meiring et al. 2006). Most DLAs have been found to be metal poor, typically far below the solar level and below the model predictions for the mean metallicity at the corresponding redshifts at which they are seen (e.g, Kulkarni et al. 2005 and references therein). We note that DLAs detected in the spectra of gamma-ray burst (GRB) afterglows are generally found to be more metal rich than their quasar absorber counterparts (e.g., Fynbo et al. 2008; Savaglio et al. 2009, 2012, and references therein). However, the sample of GRB-DLAs is much smaller than that of the QSO-DLAs. Also, most of the GRB-DLAs arise in GRB host galaxies that are likely to have high specific star formation rates and may not be typical. Also, it is very likely that the difference between GRB-DLAs and QSO-DLAs may be caused by differences in the regions of the host galaxies probed by them, with GRB-DLAs probing inner star-forming regions and QSO-DLAs probing outer regions (e.g., Fynbo et al. 2008).

The sub-DLA quasar absorption systems have until recently been largely ignored, so their contribution to the overall metal budget is not well-known. Our recent Magellan, MMT and VLT data have increased the sub-DLA Zn sample at $0.7 \leqslant z \leqslant 1.5$ by a factor of > 8, and several metal-rich sub-DLAs including some super-solar systems have been discovered (Meiring et al. 2006, 2007, 2008, 2009; Péroux et al. 2006a,b; Kulkarni et al. 2007). Evidence for the possibility of a non-negligible contribution from sub-DLAs to the metal budget came from Kulkarni et al. (2007, 2010, and references therein) based on Zn abundance measurements (see also Péroux et al. 2003a for a similar early suggestion but based on the strongly depleted element Fe).

In this work, we present high-resolution spectroscopic observations of 5 sub-DLAs taken with the Magellan Inamori Kyocera Echelle (MIKE) spectrograph on the 6.5m Clay telescope at the Las Campanas Observatory. This paper is structured in the following way: In § 2, details of our observations and data reduction techniques are discussed. § 3 discusses the methods used to determine column densities of various ions. In § 4, information on the individual absorbers from our sample are given. In § 5, we present the results from the analysis of our data, and finally in § 6, we discuss conclusions drawn from this work.

2 OBSERVATIONS AND DATA REDUCTION

The spectra of the quasars presented here were obtained over 2 separate epochs, 2008 March and 2010 May, respectively, with the Magellan Inamori Kyocera Echelle spectrograph (MIKE) (Bernstein et al. 2003) on the 6.5m Magellan Clay telescope at Las Campanas Observatory. MIKE is a double sided spectrograph consisting of both a blue and a red camera, providing for simultaneous wavelength coverage from ∼3340 Å to ∼9400 Å . The sightlines were observed in multiple exposures of 1800 to 2700 seconds each, to minimize cosmic ray defects. During data acquisition, seeing was typically $< 1''$, averaging $\sim 0.7''$. The target QSOs were observed with the $1''$x$5''$ slit and the spectra were binned 2x3 (spatial by spectral) during readout. The resolving power of the MIKE spectrograph is ∼19,000 and ∼25,000 on the red and blue sides respectively with a $1''$x$5''$ slit. Table 1 gives a summary of the observations.

We reduced the spectra using the MIKE pipeline reduction code in IDL developed by S. Burles, J. X. Prochaska, and R. Bernstein. The MIKE software makes use of the overscan region to perform bias subtraction and then flat-fields the data. The software then performs sky-subtraction and extracts the spectral orders using the traces from flat field images. The pipeline calibration code uses Th-Ar comparison lamp exposures, taken before and after each science exposure, to perform wavelengths calibration. The software also corrects for heliocentric velocities and converts the wavelengths to vacuum values. Each individual echelle order was then extracted from the IDL structure created by the pipeline software and corresponding orders from multiple exposures were combined in IRAF using rejection parameters to reduce the effects of cosmic rays. The spectra from these combined orders were then normalized individually using Legendre polynomial functions to fit the continuum. Typically, these functions were of order five or less.

Our sample consists of 5 sub-DLAs at $z > 1.7$, including 3 at $z > 2$. We focus on this redshift range, because few abundance measurements exist for sub-DLAs at these redshifts, especially at $z > 2$ (e.g., Dessauges-Zavadsky et al. 2003, 2009; Ellison & Lopez 2001; Ledoux et al. 2006; Noterdaeme et al. 2008; Pettini et al. 1994). All of the absorbers in our sample have $N_{H\ I}$ values known previously either from the Large Bright Quasar Survey or measured from the Lyα λ 1215.7 line seen in SDSS spectra. However, for the absorbers with the Lyα λ 1215.7 line falling within the spectral coverage of our MIKE observations (which is the case for all the systems except the absorber toward Q1311-0120), we report $N_{H\ I}$ values determined from our high resolution data.

3 DETERMINATION OF COLUMN DENSITIES

Column densities were determined by fitting the normalised absorption profiles using the FITS6P package (Welty et al. 1991), which has evolved from the code by Vidal-Madjar et al. (1977). FITS6P iteratively minimizes the χ^2 value between the data and a theoretical Voigt profile that is convolved with the instrumental profile. The Voigt profile fits to the absorption features seen in our data used multiple components, tailored to the individual system. For the central, core components, the Doppler parameters (b_{eff}) and radial velocities were determined from the weaker and less saturated lines, typically the Fe II λ 2374 or the Mg I λ 2852 line. For the weaker components at higher radial velocities, the b_{eff} and component velocity values were determined from stronger transitions such as Fe II $\lambda\lambda$ 2344, 2382 and Mg II $\lambda\lambda$ 2796, 2803. A set

Table 1. Summary of Observations.

QSO J2000	RA	Dec	m_V	z_{em}	z_{abs}	log $N_{H\ I}$ cm^{-2}	Exposure Time sec	Epoch	$N_{H\ I}$ Reference
Q1039-2719	10:39:21.83	-27:19:16.0	17.4	2.193	2.139	19.55±0.15	7100	2008 March 16	1
Q1103-2645	11:03:25.29	-26:45:15.7	16.0	2.145	1.839	19.52±0.04	3600	2008 March 16	1
Q1311-0120	13:11:19.26	-01:20:30.9	17.5	2.585	1.762	20.00±0.08	8100	2008 March 16	2
Q1551+0908	15:51:03.39	+09:08:49.3	17.9	2.739	2.320	19.70±0.05	6300	2010 May 06	1
Q2123-0050	21:23:29.47	-00:50:53.0	16.7	2.262	2.058	19.35±0.10	4800	2010 May 06	1

$N_{H\ I}$ References. – (1) This Work, (2) Wolfe et al. (1995)

of b_{eff} and v values were thus determined that provide reasonable fits to all of the lines observed in the system. The atomic data used in the identification of lines and profile fitting were adopted from Morton (2003).

If a multiplet was observed, the lines were fitted simultaneously. For all of the systems, the Fe II λ 2344, 2374, 2382 lines were fitted simultaneously to arrive at a set of column densities that provide reasonable fits to the spectra. Similarly, the Mg II $\lambda\lambda$ 2796, 2803 lines were also fitted together. At the resolution of our data, the Zn II λ 2026 line is blended with the Mg I λ 2026 line. The Mg I contribution to the blend was estimated using the Mg I λ 2852 line, for which fλ ∼32 times that of the Mg I λ 2026 line. The Zn II contribution was determined by fitting the rest of blend while keeping the Mg I contribution fixed. $N_{Cr\ II}$ was determined by simultaneously fitting the Cr II λ 2056 line and the blended Cr II + Zn II λ 2062 line, where the contribution from Zn II was estimated from the Zn II + Mg I λ 2026 line. See also Khare et al. (2004) for a discussion of the profile fitting scheme. In this paper we adopt the standard notation for relative abundance:

$$[X/Y] = log(N_X/N_{H\ I}) - log(X/H)_\odot,$$

Solar system abundances have been adopted from Lodders (2003).

In addition to the Voigt profile fitting method, the package SPECP, also developed by D.E. Welty, was used to determine column densities via the apparent optical depth method (AOD) (Savage & Sembach 1996). We used SPECP to measure the equivalent widths of various transitions as well. We present the rest-frame equivalent widths (W_0) of various lines in Table 2. The 1σ errors for the equivalent widths are also given and include the effect of both, the photon noise and the uncertainty in continuum placement. In the case of the non-detection of a line, the limiting equivalent width was determined from the local signal to noise ratio (S/N), and a corresponding 3σ column density upper limit was determined, assuming a linear curve of growth. Cells with "..." entries represent lines which could not be measured due to one or a combination of the following: lack of coverage, blending with Lyα forest lines, blending with atmospheric absorption bands, very poor S/N due to spectrograph inefficiency at wavelength extremes and coincidence of the line with damaged portions of the CCD.

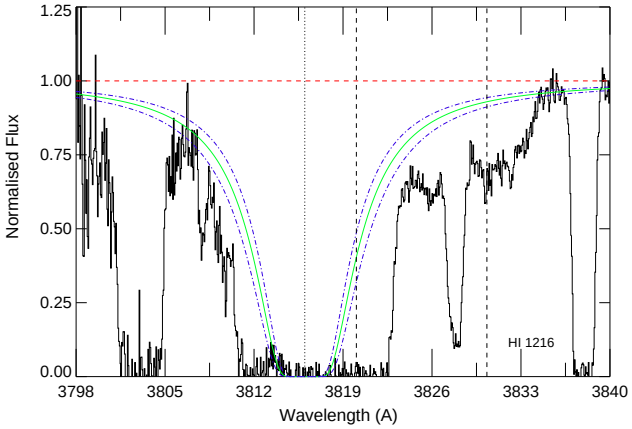

Figure 1. Lyman-α absorption feature in the z_{abs} = 2.139 system towards Q1039-2719. The solid green curve is the Voigt profile for log $N_{H\ I}$ = 19.55. The blue dotted and dashed curves above and below the green curve are Voigt profiles for log $N_{H\ I}$ = 19.40 and 19.70, respectively. The red dashed line represents the normalized continuum while the black dotted line denotes the profile center. The vertical dashed lines denote the locations of the N V $\lambda\lambda$ 1239, 1243 lines from the z_{abs} = 2.082 absorber.

4 DISCUSSION OF INDIVIDUAL OBJECTS

4.1 Q1039-2719, z_{em}=2.193

The sightline to this moderately bright BAL QSO traces a strong sub-DLA system at z_{abs} = 2.139 in addition to a weak absorber at z_{abs} = 2.082 and three broad absorption systems at z_{abs} = 1.518, 1.702, 1.757 (Srianand & Petitjean 2001). The continuum around the Lyman-α line of the sub-DLA is affected by Si IV absorption from the BAL systems at z_{abs} = 1.702 and 1.757 as well as N V absorption from the z_{abs} = 2.082 absorber. A relatively un-affected part of the spectrum redward of the Lyman-α line was used to constrain the continuum. We made use of the residual flux at ∼3815 Å to eliminate contribution from the N V $\lambda\lambda$ 1239, 1243 lines in the z_{abs} = 2.082 absorber as well as from the Lyα forest and to estimate log $N_{H\ I}$ = 19.55±0.15. The Voigt profile fit to the Lyman-α line is shown in Figure 1.

The absorption profiles of this sub-DLA system show three strong components at velocities -9, 10, and 46 km s^{-1}along with several weak satellites spanning a total ∼ 430 km s^{-1}. The sub-DLA is detected in absorption form several elements in multiple ionization stages such Mg I, Mg II, Fe II, Fe III, Si II, Si III, Si IV, C I, C II, C IV, Al II, Al III, P II, Cr II, Mn II, Ni II, S II and Zn II. Table 3 shows the column densities in individual velocity components for various ions. The Voigt profile fits to some of the lines of interest are shown in Figure 2. It is to be noted that, abundance measurements for various elements in this absorber have previously been reported by Srianand & Petitjean (2001). However, their results included measurements from the two strongest absorption components only and contributions from the weaker components, although small, were ignored. Therefore, the abundances were affected by underestimation of column densities of various ions, including Zn II and S II. To check the consistency of our abundance determinations from the MIKE spectra, we derived column densities of various ions (e.g., log N_{SII} = 14.76±0.09, log N_{FeII} = 14.69±0.06, log N_{SiII} = 14.99±0.01) using AOD measurements on

Table 2. Rest-frame equivalent widths of key metal lines from this sample. Measured values and 1σ errors are in mÅ units.

QSO	z_{abs}	Mg I 2852	Mg II 2796	Mg II 2803	Al II 1670	Al III 1854	Al III 1862	S II 1250	S II 1253	S II 1259	Si II 1526	Si II 1808
Q1039-2719	2.139	749±11	1527±54	1365±66	572±14	<933[b]	212±8	39±4	<111[b]	103±3	529±16	108±12
Q1103-2645	1.839	86±10	1034±10	768±12	...	67±10	...	6±3	<42[b]	12±4	213±5	<5
Q1311-0120	1.762	213±73	2230±53	1601±53	...	<12	<12	...	...	...	>306[a]	...
Q1551+0908	2.320	...	...	...	114±3	23±7	...	21±3	...	...	120±10	5±2
Q2123-0050	2.058	527±16	1946±6	1655±6	654±10	197±12	103±13	70±6	196±10	...	546±9	40±6
QSO	z_{abs}	Cr II 2056	Mn II 2576	Mn II 2594	Mn II 2606	Fe II 2344	Fe II 2374	Fe II 2382	Fe II 2586	Fe II 2600	Zn II[c] 2026	Zn II[d] 2062
Q1039-2719	2.139	36±6	70±9	...	<113[b]	568±5	414±15	747±15	575±13	1478±244	48±12	23±4
Q1103-2645	1.839	<3	<46[b]	<21[b]	<6	139±6	56±12	327±9	124±10	303±7	<4	<3
Q1311-0120	1.762	25±5	<10	<93[b]	...	384±49	154±25	766±53	305±53	<1281[b]	>94	>26
Q1551+0908	2.320	<6	<5	...	...	129±5	44±4	250±10	193±9	273±7	<4	<4
Q2123-0050	2.058	<3	23±3	<4	15±6	445±8	221±72	862±216	328±20	772±16	47±6	21±18

[a]This line is partially blended with Lyα forest lines. [b]This line is blended with another feature. [c]This line is blended with Mg I λ 2026. Therefore, the measured value represents the total equivalent width of the blend. However, the Mg I contribution is judged to be insignificant in all cases. [d]Since this line is blended with the Cr II λ 2062 line, the measured value represents the total equivalent width of the blended feature.

the UVES spectra from Srianand & Petitjean (2001) and compared them with our results. For most of the ions, the column densities agree within 1σ uncertainties. We also detect C II* λ 1335.7 in this sub-DLA, but the components of C II* at velocities -9 and 10 km s^{-1}are blended with the C II λ 1334 line in our MIKE spectrum. Although, we were able to measure the contribution from the component at 10 km s^{-1}using the higher resolution UVES data from Srianand & Petitjean (2001), the component at -9 km s^{-1}could not be separated from the blend, resulting in the placement of only a lower limit on the abundance of C II*. The C II* column densities listed in table 3 are from our measuremnts on the UVES data.

Photoionisation calculations for this system, as described in § 5.2, suggest that the observed metallicity ([Zn/H] = $-$0.02 dex) and depletion ([Zn/Fe] = +0.28 dex) underestimate the true values significantly. The corrected values for [Zn/H] and [Zn/Fe] were estimated to be +0.46 dex and +0.95 dex, respectively.

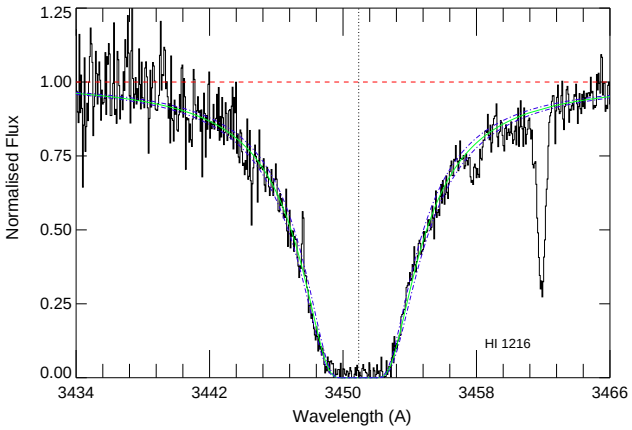

Figure 3. Same as Fig. 1, but for the Lyman-α line in the z_{abs} = 1.839 system towards Q1103-2654. The solid green curve shows the Voigt profile for log $N_{H\ I}$ = 19.52 while the blue dotted-dashed curves represent an uncertainty of 0.04.

4.2 Q1103-2645, z_{em} = 2.145

This QSO sightline probes a sub-DLA at z = 1.839 (Petitjean et al. 2000). We estimate log $N_{H\ I}$ = 19.52±0.04 for the absorber by fitting a Voigt profile to the Lyman-α line (see Figure 3). Absorption features of various elements in different ionisation stages such as Mg I, Mg II, Fe II, C II, C II*, S II, Si II, Si IV and Mn II, were detected in this system. The absorption profiles reveal 11 components ranging from -163 km s^{-1}to 39 km s^{-1}but most of the absorption comes from two main components at -49 and -12 km s^{-1}. Several key lines such as C IV $\lambda\lambda$ 1548, 1550; Al IIλ 1670 and Ni II λ 1741 fell on a damaged portion near the red end of the blue CCD of MIKE, preventing us from making reliable determination of column densities.

Table 4 summarizes the results from profile fitting analysis for this system and the velocity plots for some of the lines of interest are shown in Figure 4. There was no detection of Zn with a S/N $\sim$ 45 near Zn II λ 2026. Based on the 3σ limiting rest equivalent width, W_{rest} = 3.9 mÅ, we estimate log $N_{Zn\ II} < 11.3$ and [Zn/H] < -0.82 for this absorber. S II was detected in this system with log $N_{S\ II}$ = 13.9 and [S/H] = -0.82. We note that, [S/H] for this system has also been reported by Petitjean et al. 2000 and their value of -0.94±0.16 is consistent with our measurement within 1σ uncertainties. Ionisation modelling for this absorber indicates a moderate correction of -0.3 dex in S abundance (see section 5.2 for details). The data also show presence of Mn II λ 2576 but this line is blended with an unidentified feature. Since no other Mn II lines were detected, we could only place an upper limit on Mn abundance of this absorber.

4.3 Q1311-0120, z_{em}=2.584

This QSO sightline has a sub-DLA absorber, identified in the LBQS survey (Wolfe et al. 1995), at z = 1.762 with Lyman-α rest-frame equivalent width of 7.3±0.7 Å . The Lyman-α line was partially covered in the extreme blue order of our echelle data and because of the very poor S/N in that wavelength region, neutral hydrogen column density could not be determined using a Voigt profile fit.

Table 3. Column densities in individual velocity components for the z=2.139 absorber with log $N_{H\ I}$=19.55 in Q1039-2719. Velocities and b_{eff} values are given in units of km s^{-1}. Column densities are in units of cm^{-2} and 1σ errors in column densities are given.

Vel	b_{eff}	Mg I	Mg II	Fe II	Zn II	Ni II	C II*
-103	6.6	-	(1.79±0.57)E+12	(5.28±3.04)E+11	-	-	-
-70	9.5	-	(1.42±0.50)E+12	(6.10±3.21)E+11	-	-	-
-42	10.4	(7.23±2.83)E+11	(1.05±0.65)E+12	-	-	-	-
-9	8.7	(9.03±4.13)E+11	>6.59E+14	(7.37±0.51)E+13	-	(7.22±2.36)E+12	-[a]
10	11.5	(4.90±1.69)E+12	(2.02±0.64)E+15	(2.59±0.35)E+14	(5.31±1.32)E+11	(2.61±0.38)E+13	(1.89±0.27)E+13
46	8.5	(2.47±0.87)E+12	>4.06E+14	(1.85±0.31)E+14	(4.42±1.26)E+11	(1.89±0.33)E+13	(2.02±0.26)E+13
73	6.2	(3.28±2.56)E+11	>8.77E+12	(2.46±0.25)E+12	-	(5.63±1.92)E+12	-
86	8.0	-	>4.60E+12	(1.38±0.25)E+12	(2.23±1.17)E+11	(3.00±1.96)E+12	-
104	9.0	(3.86±2.77)E+11	(1.78±0.61)E+12	-	-	-	-
125	4.4	-	(4.71±1.09)E+12	(6.12±1.66E+11	-	-	-
140	6.4	(3.06±2.04)E+11	(1.91±0.59)E+12	(5.06±1.68)E+11	-	-	-
172	3.6	-	(3.80±0.99)E+12	(7.94±1.55)E+11	(2.46±1.04)E+11	-	-
265	5.6	-	(1.19±0.49)E+12	(4.40±1.41)E+11	-	-	-
330	6.1	-	(1.31±0.50)E=12	(3.4±1.41)E+11	-	-	-

[a] This component is blended with the C II λ 1334.5 line.

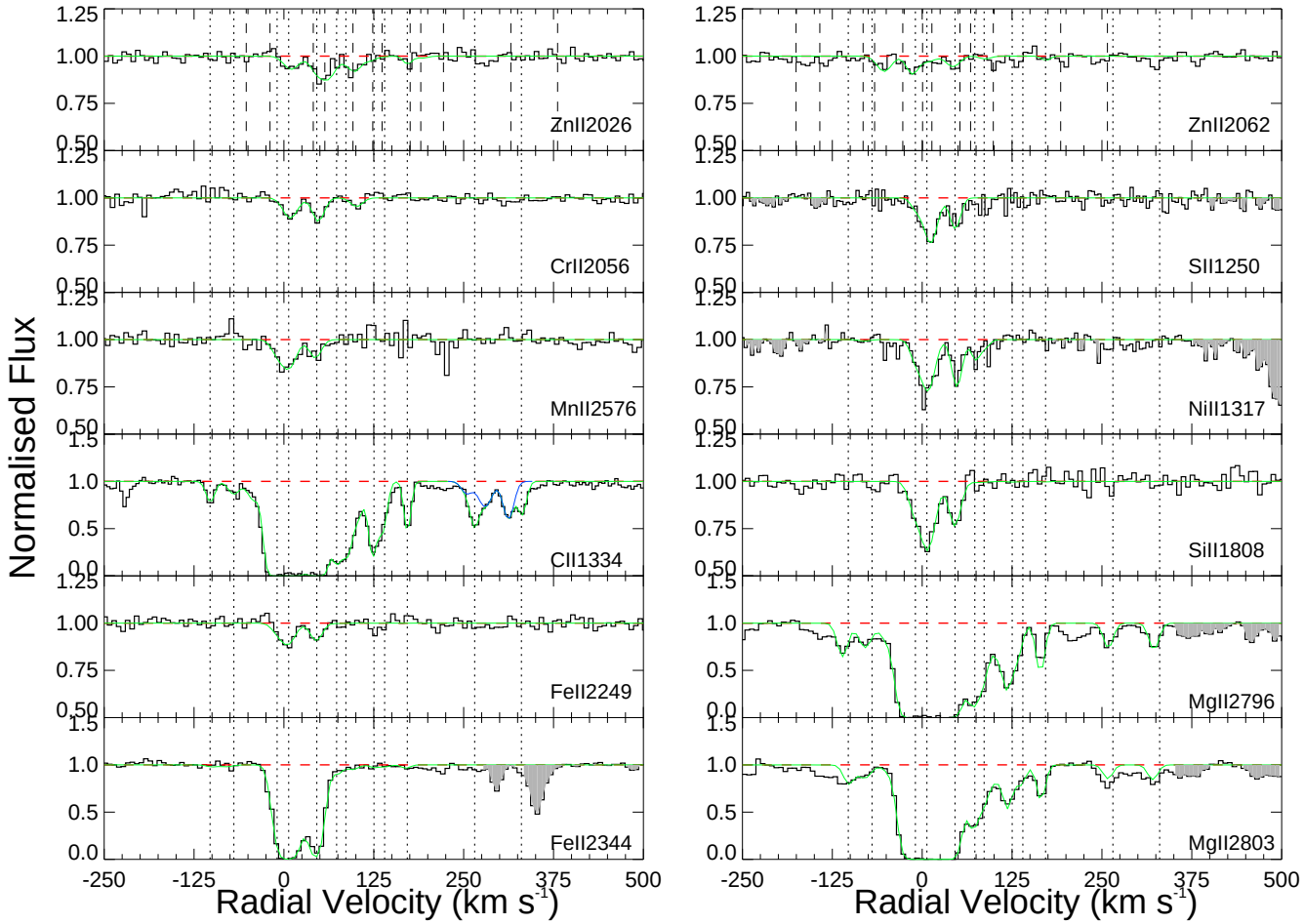

Figure 2. Velocity plots for several lines of interest in the z =2.139 system in the spectrum of Q1039-2719. The solid green line indicates the theoretical profile fit to the spectrum, and the dashed red line is the continuum level. The vertical dotted lines indicate the positions of the components that were used in the fit. In the cases of the Zn II $\lambda\lambda$ 2026,2062 lines, which have other lines nearby, the long dashed vertical lines indicate the positions of the components for Mg I (former case), and Cr II (latter case). The regions shaded in gray in some of the panels represent features unrelated to the absorption systems presented here. In the "CII 1334" panel, the solid green line represents the blend between C II λ 1334.5 and C II* λ 1335.7 lines while the solid blue line represents the contribution from C II* λ 1335.7 to this blend.

Table 4. Same as Table 3, but for the z_{abs}=1.839 absorber with log $N_{H\ I}$=19.52 in Q1103-2645

Vel	b_{eff}	Mg I	Mg II	Fe II	C II	S II
-163	2.7	-	(4.54±6.74)E+11	(2.48±7.14)E+11	(3.46±2.05)E+12	-
-139	8.2	-	(2.92±0.22)E+12	(6.08±8.34)E+11	(2.12±0.33)E+13	-
-78	11.7	-	(5.86±0.28)E+12	(1.31±0.16)E+12	(4.17±0.34)E+13	-
-67	2.2	-	-	-	(1.19±0.21)E+13	-
-49	5.9	(2.07±0.33)E+11	>3.09E+13	(7.77±0.48)E+12	>3.44E+14	(2.02±1.72)E+13
-31	6.1	(4.46±3.07)E+10	>1.60E+13	(3.52±0.40)E+12	>1.89E+14	(1.82±1.78)E+13
-12	4.5	(2.79±0.34)E+11	>5.45E+13	(1.56±0.08)E+13	>3.34E+14	(3.97±1.88)E+13
4	5.6	(6.67±3.01)E+10	-	-	(1.73±0.11)E+13	-
15	5.8	-	>5.27E+12	(3.60±0.21)E+12	>2.68E+13	-
28	4.7	(1.12±0.37)E+11	(4.33±0.33)E+12	(2.22±0.18)E+12	(2.19±0.13)E+13	-
39	6.0	-	-	-	(1.36±0.09)E+13	-

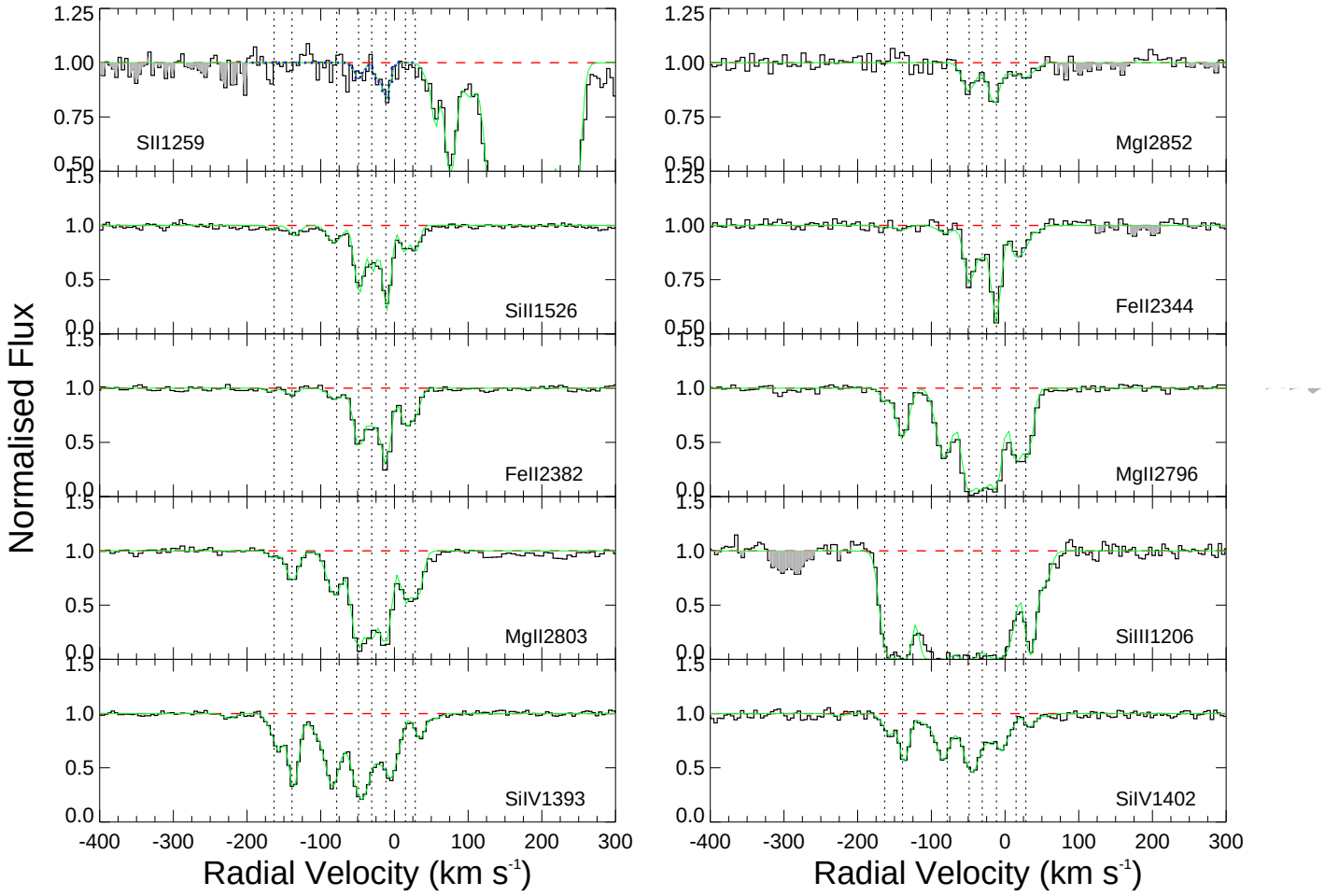

Figure 4. Same as Fig. 2, but for the z_{abs}=1.839 system in the spectrum of Q1103-2654. In the "SII 1259" panel, the solid green line represents the total contribution from the S II λ 1259.5 and the Si II λ 1260.4 lines. The contribution from S II λ 1259.5 alone is shown with the blue dotted line.

Instead, we estimate log $N_{H\ I}$ = 20.00±0.08 from the rest-frame equivalent width reported by Wolfe et al. (1995), using the curve of growth for the H I Lyman-α line. This absorber shows a relatively complex velocity structure and 12 components, spanning $\sim$ 550 km s^{-1}in velocity space were required to fit the observed absorption profiles. While most of the absorption occurs in two component clusters appearing between -5 km $s^{-1}$and 200 km s^{-1}, a weaker absorption complex, separated from the main components by more than 500 km s^{-1}, is detected in most of the strong transitions. Additional weaker components, bridging the gap between the satellite and the main absorption, are seen only in the strongest of transitions such as Fe II λ 2382 and Mg II $\lambda\lambda$ 2796, 2803. Results from the profile fitting analysis for this system are shown in Table 5.

Our data near the extreme blue end of the spectral coverage were affected by poor S/N owing to the combination of lower sen-

Table 5. Same as Table 3, but for the z_{abs}=1.762 absorber with $N_{H\ I}$=20.00 in Q1311-0120

Vel	b_{eff}	Mg I	Mg II	Fe II	Zn II	Cr II
-5	3.8	(1.80±0.63)E+11	>5.93E+012	(6.07±1.40)E+12	-	-
24	3.8	(5.01±5.24)E+10	>4.71E+013	(2.40±0.32)E+13	-	-
45	6.1	(6.25±0.86)E+11	>1.80E+014	(1.04±0.13)E+14	(1.22±0.91)E+012	(8.72±2.44)E+12
115	8.6	(1.16±0.63)E+10	(3.06±0.68)E+12	(1.16±0.29)E+12	(6.28±0.86)E+011	-
169	8.0	(8.87±6.03)E+10	>2.97E+013	(1.44±0.15)E+13	-[a]	-
184	7.3	(3.07±0.70)E+11	>2.72E+013	(4.92±1.09)E+12	-[a]	-
244	3.9	(7.91±5.26)E+10	>1.55E+013	(3.09±0.41)E+12	-[a]	-
275	7.9	-	>9.13E+012	(1.89±0.32)E+12	-	-
294	8.4	-	>8.57E+012	(1.33±0.32)E+12	(7.86±0.93)E+011	-
317	8.5	-	(2.23±0.62)E+12	(1.30±0.31)E+12	-	-
525	6.0	(2.06±0.61)E+11	>1.32E+013	(6.01±1.30)E+12	-	-
546	2.9	(2.28±0.70)E+11	>4.40E+012	(2.01±0.37)E+12	(5.76±0.82)E+011	-

[a] This component is blended with an unidentified feature.

sitivity and continuum absorption form the Lyα forest clouds. Several of the lines of interest such as S II $\lambda\lambda\lambda$ 1250, 1253, 1259; Si II λ 1304; Ni II $\lambda\lambda$ 1317, 1370; C II λ 1334; C II* λ 1336 and Si IV $\lambda\lambda$ 1393, 1402 were located in this region and therefore could not be analysed reliably. Due to the high redshift of the background QSO, even lines with higher rest wavelengths such as C IV $\lambda\lambda$ 1548, 1550 were blended with Lyα forest lines. Si II λ 1526 was partly blended with forest lines resulting in the placement of only a lower limit on Si II abundance. Zn II λ 2026 line was detected in several components in this system. However, a part of the core component structure of the line is blended with a strong unidentified feature and therefore, we report only a lower limit of log $N_{Zn\ II}$ > 12.57 and [Zn/H] > -0.06, based on the measurements of the unblended components. The component at 546 km s^{-1}, unlikely to be associated with the main absorber galaxy, contributes $\sim 15\%$ of the observed Zn II column density. However, the system is found to be metal rich ([Zn/H] > -0.14) even if contribution from this high-velocity component is ignored. This near-solar metallicity absorber also shows a high depletion with [Zn/Fe] > +1.18. Ni II λ 1741 and Al II λ 1670 were affected by cosmetic defect in the chip, however, we were able to place a lower limit on Al II abundance based on unaffected regions in the line. Velocity plots for several lines of interest are shown in Figure 5.

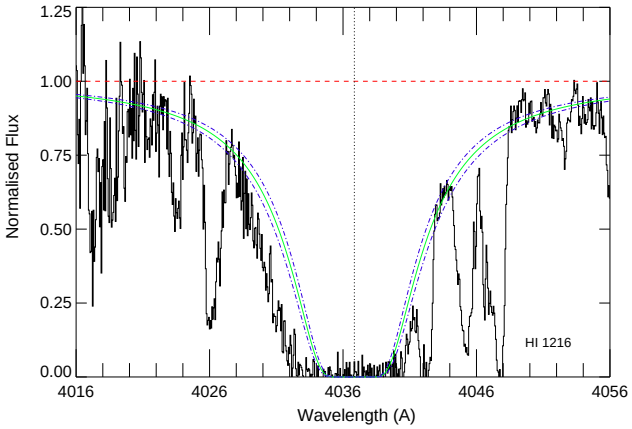

Figure 6. Same as Fig. 1, but for the Lyman-α line in the z_{abs} = 2.320 system towards Q1551+0908. The solid green curve shows the Voigt profile for log $N_{H\ I}$ = 19.70 while the blue dotted-dashed curves represent an uncertainty of 0.05.

4.4 Q1551+0908, z_{em}=2.739

This QSO sightline has a sub-DLA absorber at z = 2.320 (Noterdaeme et al. 2009). A Voigt profile fit to the Lyman-α line, shown in Figure 6, yields log $N_{H\ I}$=19.70±0.05. This sub-DLA is detected in absorption from Fe II, Fe III, Si II, Si IV, C II, C III, C IV, Al II, Al III, S II, and Ni II. Mg I λ 2852 and Mg II $\lambda\lambda$ 2796, 2803 were not covered. The observed absorption profiles show a relatively simple velocity structure for this system requiring 5 components for an adequate fit. Table 6 shows results from profile fitting analysis for this absorber. Zn II λ 2026 was not detected in our data with S/N $\sim$ 40 near the expected position of the line. Our estimate of a 3 σ limiting rest-frame equivalent width of W_{rest} = 4.38 mÅ places an upper limit on the Zn II column density at log $N_{Zn\ II}$ < 11.38 and [Zn/H] < -0.95. Measurement of the detected S II lines yield [S/H] = -0.46 and suggest significant α-enhancement with [S/Zn] > 0.49. Figure 7 shows velocity plots for several lines of interest along with their Voigt profile fits.

4.5 Q2123-0050, z_{em}=2.262

This quasar sightline traces a sub-DLA at z = 2.058 (Kaplan et al. 2010) with log $N_{H\ I}$ = 19.35±0.10. Figure 8 shows the Voigt profile we used to determine the neutral hydrogen column density for this system. A complex structure with 13 components spanning more than 350 km s^{-1}in velocity was required to model the absorption characteristics of the sub-DLA. Details of the absorption structure analysis are given in Table 7. Absorption signatures from various ions such as Mg I, Mg II, Fe II, Si II, Si IV, Al II, Al III, C II, C II*, C IV, Mn II, Ni II, S II and Zn II were detected in QSO spectrum at the sub-DLA redshift. Figure 9 shows the velocity plots of several lines of interest along with their Voigt profile fits. The metallicity of this system, based on the observed Zn II column density of log $N_{Zn\ II}$ = 12.23, is super-solar ([Zn/H] = +0.25), making it the most metal-rich sub-DLA QSO absorber known so far at z > 2 (we note here, that higher metallicities in some lower-redshift sub-DLAs have been reported by Meiring et al. 2007, 2008, 2009; Péroux et al. 2006a, 2008; Prochaska et al. 2006). In any case, due to the relatively low $N_{H\ I}$ of this absorber, it is necessary to explore the extent of ionisation effects on the metallicity value. Indeed, the observed high values of column density ratios between

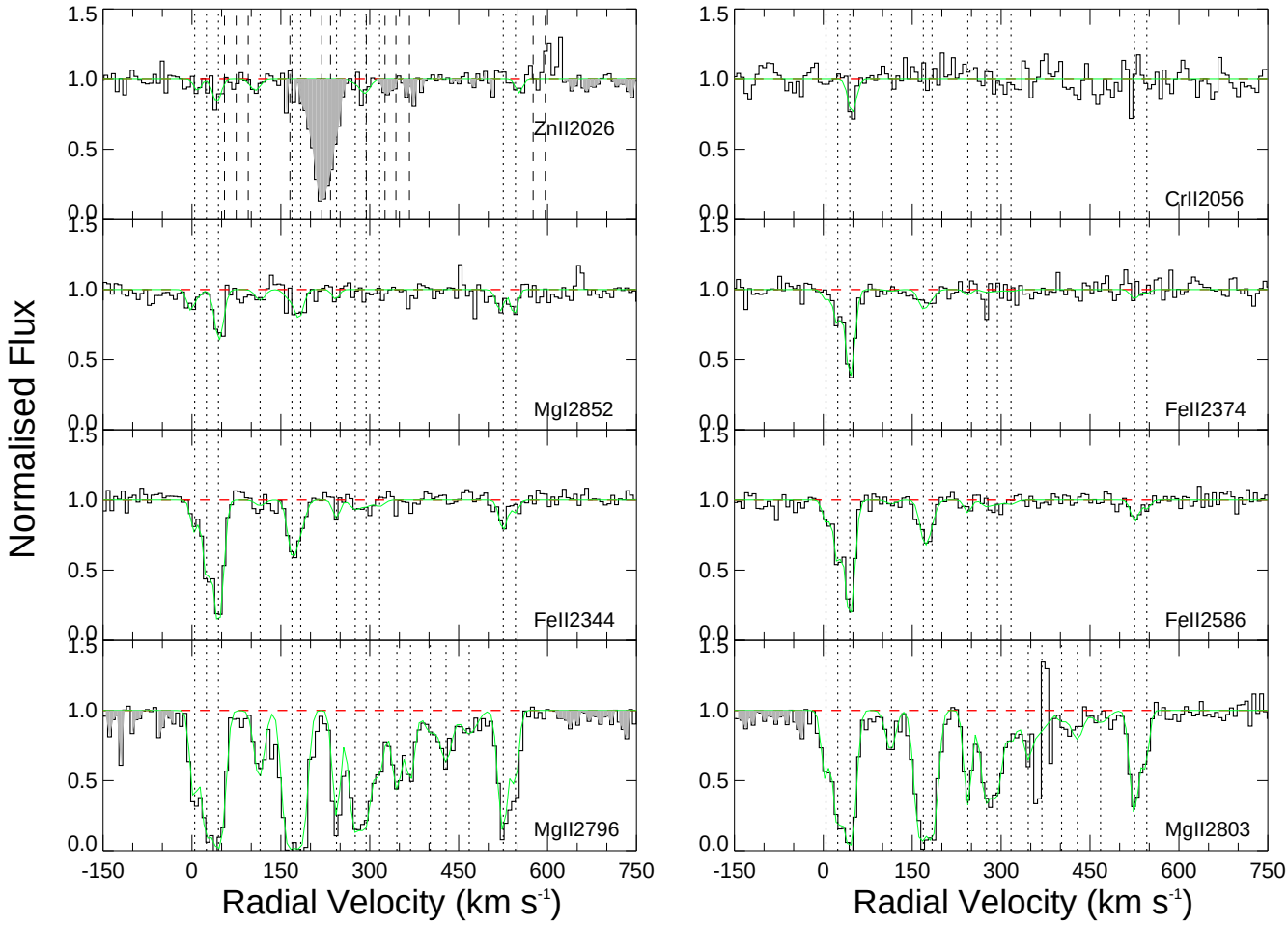

Figure 5. Same as Fig. 2, but for the z_{abs}=1.762 system in the spectrum of Q1311-0120.

Table 6. Same as Table 3, but for the z_{abs}=2.320 absorber with log $N_{H\ I}$=19.70 in Q1551+0908

Vel	b_{eff}	Fe II	Si II	C II	Al II	S II
-11	3.1	(4.54±0.94)E+012	(1.46±0.49)E+13	(3.49±2.20)E+14	(6.00±1.13)E+11	-
-2	7.0	(1.99±0.28)E+013	(3.93±0.48)E+13	>2.37E+14	(1.73±0.13)E+12	(9.72±3.28)E+13
15	5.8	(1.10±0.24)E+013	(2.20±0.31)E+13	>1.45E+14	(8.33±0.71)E+11	(1.02±0.28)E+14
32	3.0	(3.21±2.26)E+011	(3.14±1.85)E+12	(2.49±1.04)E+12	(6.56±4.15)E+10	(4.72±2.38)E+13
85	7.2	(6.04±2.57)E+011	(2.95±1.28)E+12	-	-	-

adjacent ions such as Al III/Al II, Si III/Si II, and Al III/Fe II in this absorber suggest a high level of ionisation. Our photoionisation calculations indicate a correction of +0.59 dex for [Zn/H] (See sec. 5.2 for further details).

5 RESULTS

5.1 Total Column Densities

The results of the Voigt profile fits to various absorption features from the sub-DLAs in this sample are summarised in Table 8. Log of the total column densities (sum of the column densities in the individual components determined via the profile-fitting method) for various ions are listed in this table. Column densities, determined using the apparent optical depth (AOD) method to check the consistency of our fits and are also listed in Table 8. In most cases, the column densities from the profile fitting and AOD methods agree to within the error bars, especially for the weak and unsaturated lines. Cells with "..." entries have undetermined column densities due to the reasons described in § 3. Total Zn II column density from Table 8 and the corresponding $N_{H\ I}$ value for an absorber were used to determine its metallicity, [Zn/H]. Abundances of S and Fe relative to H were determined likewise. The metallicities and other relative abundances for the observed systems are listed in Table 9. Zn was detected in three of the sub-DLA absorbers in our sample, and for the rest of the systems we place 3σ upper limits on the Zn abundance. All of the absorbers for which Zn was detected, were found to be metal-rich ([Zn/H] = -0.02 for Q1039-2719 at z_{abs} = 2.139;

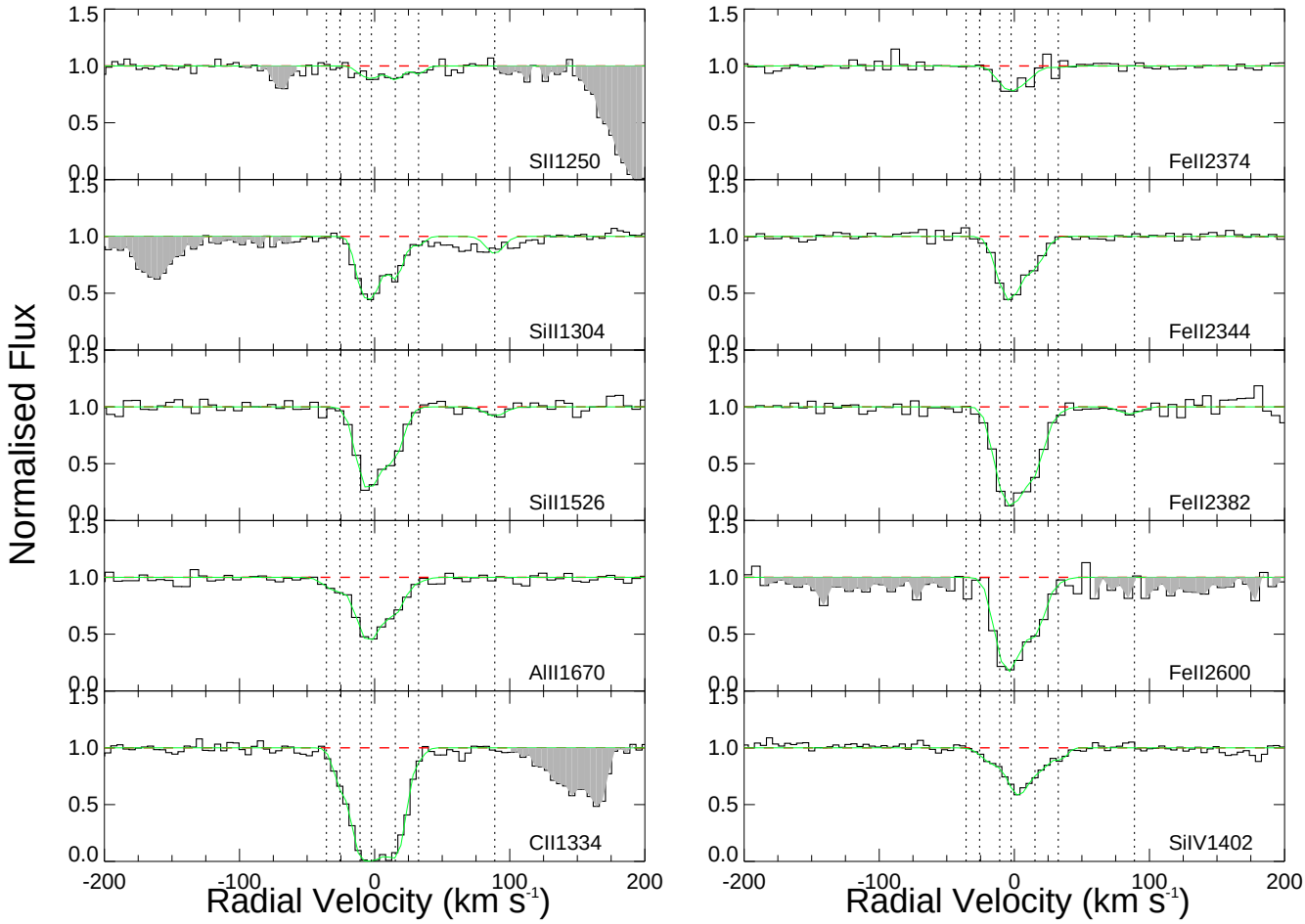

Figure 7. Same as Fig. 2, but for the z_{abs}= 2.320 system in the spectrum of Q1551+0908.

Table 7. Same as Table 3, but for the z_{abs}=2.058 absorber with log $N_{H\ I}$=19.35 in Q2123-0050

Vel	b_{eff}	Mg I	Fe II	Si II	S II	Zn II	Mn II
-116	5.8	(2.20±0.29)E+11	(8.84±0.45)E+12	(2.69±1.10)E+13	-	-	-
-101	1.4	-	(2.38±0.42)E+12	(4.04±8.30)E+13	-	-	-
-86	5.1	(1.22±0.26)E+11	(5.16±0.38)E+12	(1.87±0.88)E+13	-	-	-
-57	3.3	(1.71±0.43)E+11	(5.11±0.40)E+12	(1.07±0.73)E+13	-	-	-
0	8.2	-	(1.08±0.26)E+12	(3.06±0.56)E+12	-	-	-
32	5.6	-	(1.28±0.24)E+12	(4.87±0.56)E+12	-	-	-
74	2.3	(8.35±2.6)E+10	(2.77±0.45)E+12	(6.76±0.73)E+12	(5.64±1.50)E+13	-	-
91	5.1	(2.94±0.32)E+11	(7.65±0.53)E+12	(2.17±0.11)E+13	(1.19±0.17)E+14	(9.56±9.00)E+010	-
128	6.6	(2.12±0.1E)+12	(3.35±0.30)E+13	(3.71±0.35)E+14	(3.87±0.22)E+14	(7.88±1.11)E+011	(4.17±1.40)E+011
148	7.3	(1.11±0.06)E+12	(1.99±0.09)E+13	(8.51±4.10)E+13	(1.24±0.17)E+14	-	(5.16±1.44)E+011
175	4.4	(3.21±0.35)E+11	(7.71±0.55)E+12	(2.06±0.12)E+13	(5.77±1.90)E+13	(6.48±1.08)E+011	(3.44±1.28)E+011
212	4.1	(7.19±0.59)E+11	(2.69±0.17)E+13	(5.96±0.47)E+13	(1.12±0.10)E+14	-	-
240	4.9	(9.43±2.6)E+10	(9.82±2.50)E+11	(2.36±0.49)E+12	(6.08±1.80)E+13	-	-

> -0.06 for Q1311-0120 at z_{abs} = 1.762 and $+0.25$ for Q2123-0050 at z_{abs} = 2.058). These absorbers are among the most metal-rich sub-DLAs at $z \gtrsim 1$ and are the only near-solar or super-solar metallicity sub-DLA QSO absorbers at $z \gtrsim 2$. The Zn abundance upper limits for Q1103-2645 (z_{abs} = 1.839) and Q1551+0908 (z_{abs} = 2.320) place their metallicities at < -0.82 and < -0.95, respectively. Sulphur was detected in these two systems and their metallicities based on S abundances are -0.82 (for Q1103-2645) and -0.46 (for Q1551+0908).

Table 9 also lists the abundance ratios of various elements along with the corresponding solar values from Lodders (2003). In addition to the [Zn/Fe] ratio, often used as an indicator of dust depletion, [S/Zn], [Si/Fe], [Cr/Fe] and [Mn/Fe] are listed. As seen from the values listed in Table 9, systems with relatively high

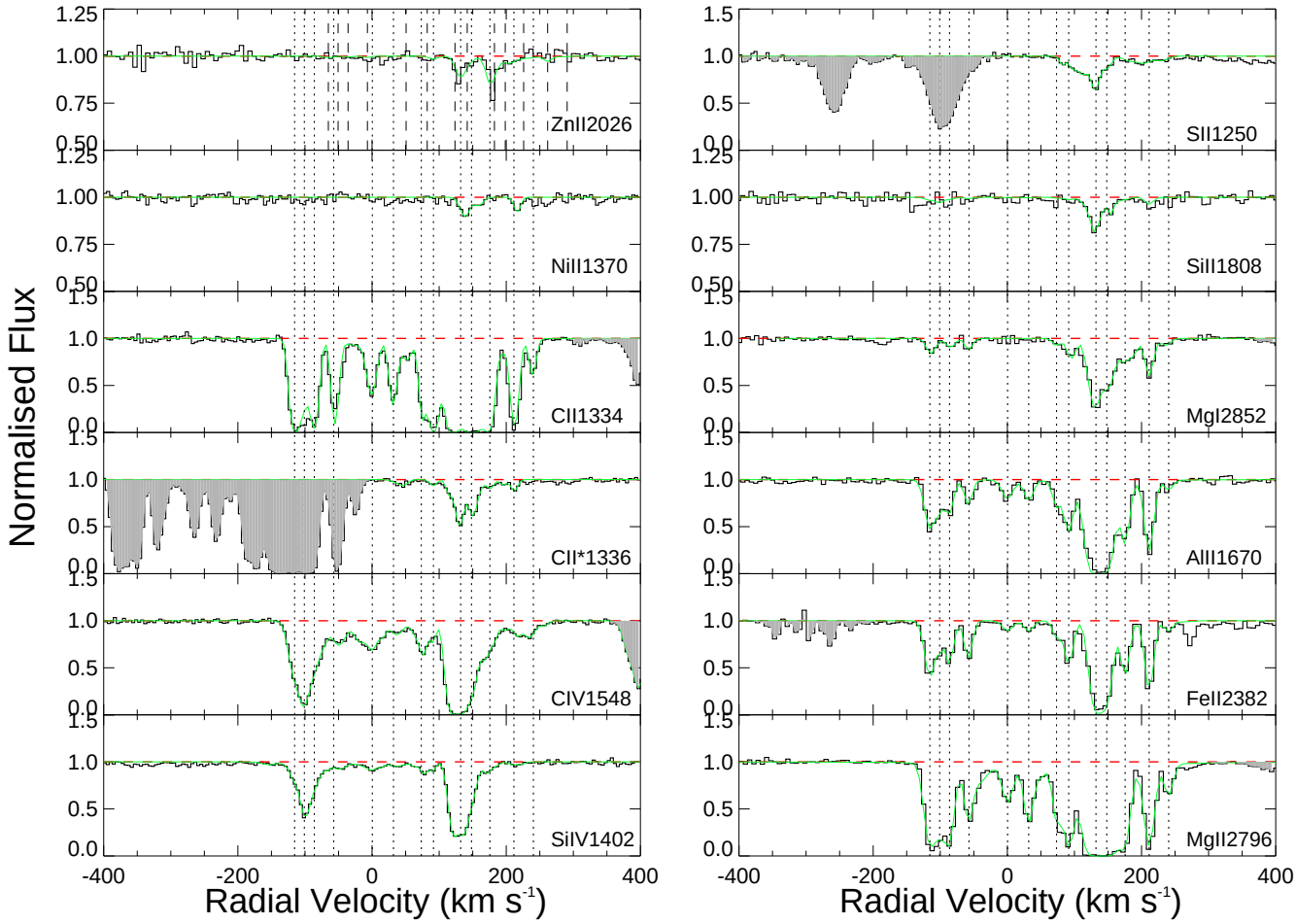

Figure 9. Same as Fig. 2, but for the z_{abs}=2.058 system in the spectrum of Q2123-0050. In the "CII*1336" panel, the shaded region represents absorption from the C II λ 1334.5 line.

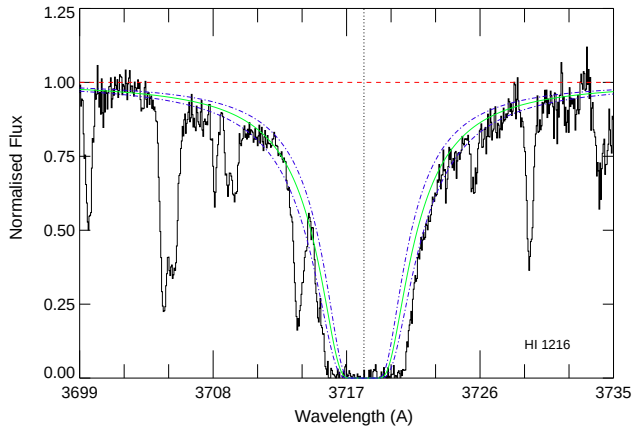

Figure 8. Same as Fig. 1, but for the Lyman-α line in the z_{abs} = 2.058 system towards Q2123-0050. The solid green curve shows the Voigt profile for log $N_{H\ I}$ = 19.35 while the blue dotted-dashed curves represent an uncertainty of 0.10.

metallicities show relatively higher dust depletion which agrees with trends found in earlier investigations. We also find evidence of α-enhancement, based on the [S/Zn] ratio, in two of the absorbers (toward Q1551+0908 and Q2123-0050) in our sample. Table 9 also lists column density ratios between elements in different ionisation stages, which may provide information about ionisation in these systems.

5.2 Photoionisation Modelling and Ionisation Corrections

The gas in the high H I column density absorbers is usually expected to be largely neutral due to the self-shielding of photons with $h\nu > 13.6$ eV. Zn and S in these systems are expected to be predominantly singly ionised. Consequently, the metallicities reported for such high $N_{\rm H\ I}$ absorbers are estimated from $N_{\rm ZnII}/N_{\rm HI}$ or $N_{\rm SII}/N_{\rm HI}$ ratios. For absorbers with lower $N_{\rm H\ I}$, such estimates may not be correct if they have non-negligible contributions from higher ionisation stages. Several studies investigating the effect of ionisation in DLAs (e.g., Howk & Sembach 1999; Vladilo et al. 2001; Prochaska et al. 2002) have found that in most cases the ion-

Table 8. Total column densities for the absorbers in this sample. Cells with "..." entries represent undetermined column densities.

QSO	z_{abs}	log $N_{H\ I}$ cm^{-2}	log $N_{Mg\ I}$ cm^{-2}	log $N_{Mg\ II}$ cm^{-2}	log $N_{Al\ II}$ cm^{-2}	log $N_{Al\ III}$ cm^{-2}	log $N_{C\ II}$ cm^{-2}	log $N_{C\ II*}$ cm^{-2}	log $N_{C\ IV}$ cm^{-2}	log $N_{S\ II}$ cm^{-2}
Q1039-2719	2.139	19.55±0.15	13.02±0.09	>15.49	>13.88	13.53±0.02	>15.78	>13.35	...	14.76±0.03
AOD			12.98±0.01	>15.16	>13.66	13.52±0.01	>15.08			14.75±0.04
Q1103-2645	1.839	19.52±0.04	11.86±0.05	>14.08	...	12.74±0.07	>15.01	>12.93	...	13.89±0.17
AOD			11.84±0.05	>13.79		12.64±0.06	>14.69	>12.30		13.73±0.14
Q1311-0120	1.762	20.00±0.08	12.27±0.04	>14.55	>13.03	<11.85	...	...	...	...
AOD			12.25±0.14	>14.15	>12.90					
Q1551+0908	2.320	19.70±0.05	...	...	12.55±0.02	12.05±0.08	>14.87	<12.17	13.81±0.02	14.43±0.09
AOD					12.53±0.01	12.14±0.13	>14.51		13.77±0.03	14.47±0.07
Q2123-0050	2.058	19.35±0.10	12.74±0.01	>14.50	>15.24	13.45±0.07	>15.99	>13.82	>14.62	15.05±0.02
AOD			12.72±0.01	>14.27	>13.47	13.14±0.02	>15.16	>13.80	>14.57	15.01±0.04

QSO	z_{abs}	log $N_{H\ I}$ cm^{-2}	log $N_{Si\ II}$ cm^{-2}	log $N_{Si\ III}$ cm^{-2}	log $N_{Si\ IV}$ cm^{-2}	log $N_{Cr\ II}$ cm^{-2}	log $N_{Mn\ II}$ cm^{-2}	log $N_{Ni\ II}$ cm^{-2}	log $N_{Fe\ II}$ cm^{-2}	log $N_{Zn\ II}$ cm^{-2}
Q1039-2719	2.139	19.55±0.15	15.30±0.03	>14.48	>14.50	13.07±0.04	12.48±0.06	13.79±0.04	14.72±0.04	12.16±0.07
AOD			15.31±0.05	>14.30	>14.50	12.99±0.07	12.54±0.06	13.75±0.07	14.74±0.02	12.40±0.08
Q1103-2645	1.839	19.52±0.04	14.07±0.02	>14.64	13.84±0.01	<11.91	<12.46	<12.34	13.54±0.02	<11.33
AOD			14.00±0.01	>14.12	13.82±0.01		<12.37		13.52±0.04	
Q1311-0120	1.762	20.00±0.08	>14.38	...	...	12.94±0.12	<11.65	...	14.23±0.35	>12.57
AOD			>14.26			12.87±0.09			14.09±0.06	>12.75
Q1551+0908	2.320	19.70±0.05	13.91±0.04		13.34±0.01	<12.15	<11.40	13.01±0.32	13.56±0.05	<11.38
AOD			13.97±0.02	>13.69	13.31±0.02			13.11±0.04	13.57±0.07	
Q2123-0050	2.058	19.35±0.10	14.89±0.06	>14.72	>13.99	<11.90	12.11±0.08	13.12±0.08	14.09±0.01	12.23±0.06
AOD			14.85±0.06	>14.15	>13.95		12.04±0.06	13.01±0.10	14.01±0.01	12.44±0.06

Table 9. Observed values of relative abundances and abundance ratios for the systems in this sample. The solar value of the ratios are given in the first row.

QSO	z_{abs}	log $N_{H\ I}$	[Zn/H]	[S/H]	[Fe/H]	[S/Zn]	[Zn/Fe]	[Si/Fe]	[Cr/Fe]
log $(X/Y)_\odot$			−7.37	−4.81	−4.53	+2.56	−2.84	+0.07	−1.82
Q1039-2719	2.139	19.55±0.15	−0.02±0.17	+0.02±0.15	−0.30±0.16	+0.04±0.08	+0.28±0.08	+0.51±0.05	+0.17±0.05
Q1103-2645	1.839	19.52±0.04	<−0.82	−0.82±0.19	−1.45±0.04	>+0.01	<+0.62	+0.46±0.03	<+0.19
Q1311-0120	1.762	20.00±0.08	>−0.06	...	−1.24±0.09	...	>+1.18	>+0.08	+0.53±0.13
Q1551+0908	2.320	19.70±0.05	<−0.95	−0.46±0.10	−1.61±0.07	>+0.49	<+0.66	+0.28±0.06	<+0.41
Q2123-0050	2.058	19.35±0.10	+0.25±0.12	+0.51±0.10	−0.73±0.10	+0.26±0.06	+0.98±0.06	+0.73±0.06	<−0.38

QSO	z_{abs}	log $N_{H\ I}$	[Mn/Fe]	Al III/Al II[a]	Fe II/Al III[a]	Mg II/Al III[a]	Mg II/Mg I[a]	Si III/Si II[a]	Si IV/Si II[a]
log $(X/Y)_\odot$			−1.97						
Q1039-2719	2.139	19.55±0.15	−0.27±0.07	<−0.35	+1.20±0.04	>+1.97	>+2.48	>−1.01	>−0.81
Q1103-2645	1.839	19.52±0.04	<+0.89	...	+0.90±0.06	>+1.44	>+2.22	>+0.05	−0.23±0.02
Q1311-0120	1.762	20.00±0.08	<−0.61	<−1.05	>+2.38	>+2.70	>+2.28	...	...
Q1551+0908	2.320	19.70±0.05	<−0.19	−0.41±0.14	+1.42±0.14	...	...	>−0.23	−0.58±0.04
Q2123-0050	2.058	19.35±0.10	−0.01±0.08	<−0.01	+0.64±0.07	>+0.82	>+1.53	>−0.73	>−0.89

[a]Ratio of column densities.

isation correction factor, defined here as

$$\epsilon = [X/H]_{total} - [X^+/H^0],$$

where $[X/H]_{total}$ include contributions from all ionisation stages, is $\lesssim 0.2$ dex for most elements. Sub-DLA systems, by virtue of lower H I in them, might be expected to show higher level of ionisation. However, it has previously been shown that the ionisation corrections are, in general, small for the sub-DLA systems as well (e.g., Dessauges-Zavadsky et al. 2003; Meiring et al. 2007, 2008).

To estimate the effect of ionisation on the sub-DLA abundances presented here, we carried out photoionisation modelling of these systems using version 13.01 of the CLOUDY photoionisation code (Ferland et al. 2013). The models were generated assuming that the ionising radiation incident on the gas cloud is a combination of extragalactic UV background and a radiation field produced by O/B type stars. The extragalactic UV background is adopted from Haardt & Madau (1996) and Madau, Haardt, & Rees (1999), evaluated at the redshift of the absorber. The O/B type stellar radiation field is based on a Kurucz model stellar spectrum for a temperature of 30,000 K. These radiation fields were mixed in equal parts to generate the incident radiation field. It has been suggested that the contribution from local sources to the ionisation of DLA systems may not be negligible in comparison with the background ionising radiation (Schaye 2006). In addition, we also in-

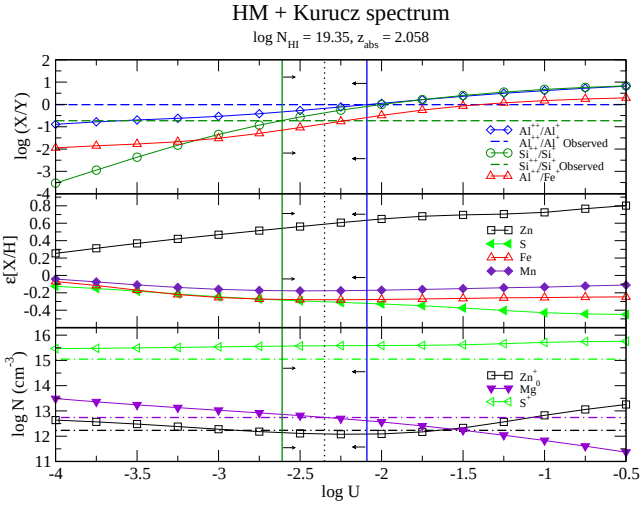

Figure 10. Results of the photoionisation simulations for the sub-DLA toward Q2123-0050. The top panel shows the simulated logarithmic column density ratios of Al^{++}/Al^{+}, Si^{++}/Si^{+} and Al^{++}/Fe^{+}, plotted vs. the ionisation parameter. The observed upper limit for Al^{++}/Al^{+} and the lower limit for Si^{++}/Si^{+} are also plotted in the same panel. The lower and upper limits on log U, determined by comparing the simulated and observed data, are represented by the vertical solid green and blue lines, respectively. The vertical dotted line represents the mean of these limits. The panel in the middle shows the ionisation correction factors for Zn, S, Mn and Fe abundances in dex. The bottom panel shows column density predictions from a grid of models with the corrected metallicity incorporated in them. The comparison of the predictions with the observed column densities of Zn^{+} and Mg^{0}, also shown in the bottom panel using horizontal dot-dashed black and purple lines, respectively, suggests that the adopted ionisation correction to metallicity is fairly reasonable.

clude the cosmic microwave background at the appropriate redshift of the absorber, and the cosmic ray background in our simulation. We note however, that radiation from local shocks originating from white dwarfs compact binary systems or supernovae was not included in our models. For each of our absorbers, grids of photoionisation models were produced by varying the ionisation parameter, defined as

$$U = \frac{n_\gamma}{n_H} = \frac{\Phi_{912}}{cn_H}$$

(where Φ_{912} is the flux of radiation with hν > 13.6 eV), from 10^{-6} to 1. The models assumed the solar abundance pattern for the absorbers and were tailored to match the observed $N_{H\ I}$ and the observed metallicity based on $N_{Zn\ II}$. Column density ratios between various ions resulting from these grids of simulation were then compared with the observed values (see Table 9) to constrain the ionisation parameter and derive the ionisation correction values. We note, however, that ionisation in the gas depends strongly on the shape of the ionising spectrum and our assumption for the incident spectrum is one among many possibilities. Given the assumptions described above, we can only arrive at some general conclusions regarding the strength of ionisation in the gas.

With log $N_{H\ I}$ = 19.35, the sub-DLA in the spectrum of Q2123-0050 is the lowest $N_{H\ I}$ system in our sample. The observed ratios of column densities in higher ionisation stages to those in the lower ionisation stages are relatively high in this system, suggesting significant ionisation in the absorbing gas. Column density ratios of the adjacent ions of the same element are more reliable observational constraints than the ratios involving different elements as the latter may be affected by differential depletion or intrinsic nucleosynthetic differences. Al and Si were the elements detected in this system with multiple ionisation stages. We used the observed lower limit of the N_{Si++} to N_{Si+} ratio to obtain a lower limit on the ionization parameter at log U > -2.6. Furthermore, the observed upper limit on N_{Al++}/N_{Al+} implies log U < -2.1. These results suggest that the observations underestimate the metallicity significantly as the ionisation correction for [Zn/H] ranges between +0.54 dex to +0.63 dex. We adopt the correction to metallicity to be +0.59 dex derived for log U = -2.35, the mean value of the ionisation parameter range described above. The corrections for [Fe/H] and [Mn/H] are derived to be -0.28 dex and -0.18 dex, respectively, suggesting a corrected value of +0.09 dex for [Mn/Fe]. The suggestion that the true depletion is much higher than observed (based on Zn II and Fe II) in a significantly ionised system (Meiring et al. 2008) seems to be true for this system as the corrected [Zn/Fe] is $\sim$ +0.9 dex higher than the observed [Zn/Fe] = +0.98 dex. Figure 10 describes ionisation modelling results for this system.

The observed limits on N_{Al++}/N_{Al+} and N_{Si++}/N_{Si+} in the log $N_{H\ I}$ = 19.55 absorber toward Q1039-2719 suggest -3.1 < log U < -2.7. This implies a correction for [Zn/H] between +0.45 dex and +0.51 dex. The ionisation corrections for [Zn/H], [S/H], [Mn/Fe] and [Zn/Fe], derived at the mean log U = -2.9, are +0.48 dex, -0.20 dex, +0.08 dex and +0.67 dex, respectively.

Adjacent-ion column density ratios in the log $N_{H\ I}$ = 19.52 absorber toward Q1103-2645 also suggest moderate ionisation correction to the observed abundances. The observed lower limit on the N_{Si++} to N_{Si+} ratio allowed us to place a lower limit on the ionisation parameter at log U > -3. As the Al II line was not detected in this system, we used the N_{Al++}/N_{Fe+} ratio to further constrain the ionisation parameter at log U = -2.6. The predicted correction for [S/H] was found to be -0.31 dex. Mn and Fe abundances were only mildly affected by ionisation as shown by the estimated correction factors of -0.10 dex and -0.13 dex for [Mn/H] and [Fe/H], respectively. We note that using the Al^{++}/Fe^{+} ratio to estimate the ionisation parameter may introduce uncertainties due to differential depletion or nucleosynthetic differences between the elements (see Meiring et al. 2007 for a more detailed discussion on the use of adjacent ion ratios in photoionisation modelling).

The models for the absorbers toward Q1551+0908 and Q1311-0120 suggest little effect of ionisation on the observed abundances. For the log $N_{H\ I}$ = 19.70 system in the spectrum of Q1551+0908, the observed value of N_{Al++}/N_{Al+} = -0.41 suggests corrections of only -0.16 dex and -0.10 dex for [S/H] and [Fe/H], respectively. With log $N_{H\ I}$ = 20.00, the sub-DLA toward Q1311-0120 is the highest $N_{H\ I}$ sub-DLA in our sample and is found to be the least ionised. The limits on the column density ratios between Al^{++}/Al^{+} and Si^{++}/Si^{+} constrain the ionisation parameter between -4.7 dex and -4.3 dex, limiting the correction for [Zn/H] between +0.10 dex and +0.18 dex (+0.14 dex at the mean ionisation parameter of log U = -4.5). The ionisation corrections for [Mn/H] and [Fe/H] were found to be negligibly small.

5.3 Metallicity Evolution

We examine metallicity evolution in sub-DLAs and DLAs, by combining our data with those from the literature (Akerman et al. 2005; Battisti et al. 2012; Boissé et al. 1998; Centurión et al. 2003; de la Varga et al. 2000; Dessauges-Zavadsky et al. 2003, 2009; Ellison & Lopez 2001; Fynbo et al. 2011; Ge et al. 2001; Khare et al. 2004; Kulkarni et al. 1999, 2005; Ledoux et al. 2006;

Lopez et al. 1999, 2002; Lopez & Ellison 2003; Lu et al. 1995, 1996; Meiring et al. 2006, 2007, 2008, 2009; Meyer & York 1992; Meyer et al. 1995; Molaro et al. 2000; Nestor et al. 2008; Noterdaeme et al. 2008; Péroux et al. 2002, 2006a,b, 2008; Petitjean et al. 2000; Pettini et al. 1994, 1997, 1999, 2000; Prochaska & Wolfe 1998, 1999; Prochaska et al. 2001, 2002, 2003a,c; Rafelski et al. 2012; Rao et al. 2005; Srianand & Petitjean 2001). Rafelski et al. (2012) presented metallicity vs. redshift relation for a larger DLA sample (242 systems) but many of their metallicity measurements come from Si and Fe, elements prone to depletion. For our analysis, we prefer not to use Si or Fe, so as to avoid the ambiguity in estimating dust depletion corrections. Instead, we use measurements of Zn or S (in cases where Zn was not detected), since these nearly undepleted elements provide the most direct gas-phase metallicity estimates. For systems with no detection of Zn and S, upper limits on Zn have been used and were treated with survival analysis. N_{HI}-weighted mean metallicity versus look-back time relations for DLAs and sub-DLAs were determined using the procedures described in Kulkarni & Fall (2002). Figure 11 shows the relations for 195 DLAs and 68 sub-DLAs in the current sample. The DLA and sub-DLA sample are divided into 12 and 6 bins, respectively. The DLA bins contain 16 or 17 systems each, while the sub-DLA bins contain 11 or 12 systems each.

Consistent with the findings from previous studies, the current sample shows the DLAs to be generally metal poor at all redshifts probed. The sub-DLA global mean metallicity appears to be higher than that of DLAs at all redshifts for which both DLA and sub-DLA observations are available ($0 \lesssim z \lesssim 3$). We note that although few metal rich DLAs have indeed been observed (e.g., Fynbo et al. 2011; Khare et al. 2004; Nestor et al. 2008; Péroux et al. 2006b), their fraction is much lower than that of the metal rich sub-DLAs. The data also show evidence for only a weak redshift evolution in the metallicity of DLAs. The bold solid and dashed curves in Fig. 11 show the best linear-regression fits to the N_{HI}-weighted mean metallicity vs. redshift data for sub-DLAs and DLAs, respectively. The linear regression estimates of the intercepts, 0.04 ± 0.23 for sub-DLAs and -0.70 ± 0.11 for DLAs, differ at 2.9 σ level. The slope of the fit is estimated to be -0.32 ± 0.13 for sub-DLAs, marginally higher than the slope, -0.19 ± 0.05, for DLAs. It is necessary to increase the sub-DLA sample size and to expand the sub-DLA sample at $z > 3$ to better constrain whether or not sub-DLAs evolve faster than DLAs.

Figure 11 also shows the comparison of the observations with theoretical model predictions for evolution of global interstellar metallicity. The mean interstellar metallicity from the chemical evolution model of Pei et al. (1999) is shown using the light dot-dashed curve (PFH 1999). This model calculates the coupled global evolution of stellar, gaseous, and metal contents of galaxies by incorporating the optimum fit for the cosmic infrared background intensity and observational constraints derived from optical galaxy surveys and the comoving H I density inferred from DLA data. The light dot-double-dashed curve (SPF 2001) represents the mean metallicity evolution of interstellar cold gas predicted by a semi-analytic model of galaxy formation in the cold dark matter merging hierarchy by Somerville et al. (2001). This model assumes a constant-efficiency quiescent star formation in addition to starbursts triggered by galaxy mergers. It is evident from Fig. 11, that the metallicity evolution in sub-DLAs is consistent with the chemical evolution models over most of the redshift range probed so far, and especially at low redshifts, reaching solar level at $z = 0$. The sub-DLA trend bears a closer resemblance with the merger driven 'collisional starburst model' by Somerville et al. (2001). On the other hand, the DLA data are in poor agreement with the model predictions and DLA metallicity reaches only $\sim$ 1/5th of the solar value at $z = 0$. The DLA trend becomes consistent with PFH 1999 only at $z \gtrsim 2$. Some recent studies (e.g., Davé & Oppenheimer 2007) predict a low DLA metallicity at $z = 0$, but do not correctly predict the higher redshift DLA metallicities. The difference in the metallicity evolution trends in DLAs and sub-DLAs may suggest that the galaxies traced by these absorbers follow separate evolutionary tracks established as early as $\sim$2 Gyrs after the Big Bang. However, given the small difference between the slopes of the trends, the observed difference can extend further back in time. Sub-DLA data at redshifts higher than 3 are essential to provide further constraints on the epoch of establishment of these distinct evolutionary tracks.

Comparing the metallicities for DLAs and sub-DLAs with those for galaxies detected in emission can provide clues to the understanding of the nature of the absorbing galaxies. It is well-known that galaxies detected in emission show a correlation between their stellar mass and the gas metallicity (e.g., Tremonti et al. 2004; Erb et al. 2006). Furthermore, the mass-metallicity relation is found to evolve with redshift. Maiolino et al. (2008) found that for star forming galaxies at $M_* \sim 10^{10}\ M_\odot$, the metallicity at $z \sim 2.2$ is lower by a factor of about 2.5 with respect to that at $z \sim 0$. The drop is less steep for more massive galaxies, indicating that the latter got enriched at earlier epochs, consistent with the mass-downsizing scenario. Comparing Fig. 9 of Maiolino et al. (2008) with our Fig. 11, the sub-DLA trend seems to resemble that for star forming galaxies with $M_* \sim 10^{10}\ M_\odot$. The trend for DLAs, however, does not resemble any of the trends found by Maiolino et al. (2008) for star forming galaxies with $9 < \log M_*/M_\odot < 11$, suggesting that DLA host galaxies have not undergone much star formation and chemical enrichment even by the current epoch. This is consistent with the observed agreement of DLA metallicity distribution with that for the Milky Way halo stars, suggesting that most DLAs are not representative of the disks of Milky Way-type galaxies (e.g., Pettini 2004).

5.4 [Mn/Fe]-Metallicity Correlation

The condensation temperatures of Mn and Fe being similar, the abundance ratio between these two elements is expected to be primarily governed by differences in their nucleosynthesis. The Mn abundance shows a strong metallicity dependence in Milky Way stars. [Mn/Fe] is also found to be correlated with [Fe/H] in the sense that [Mn/Fe] increases with increasing [Fe/H] (e.g., Nissen et al. 2000; McWilliam et al. 2003; Gratton et al. 2004). A similar trend between [Mn/Fe] and [Zn/H] is also seen to be present in DLAs and sub-DLAs (e.g., Meiring et al. 2009). In Figure 12, we plot [Mn/Fe] versus [Zn/H] for the absorbers in this sample, along with the data for DLAs and sub-DLAs taken from the literature. Data from Reddy, Lambert, & Prieto (2006) for Milky Way stars and the interstellar abundance data for SMC from Welty et al. (2001) are also shown overlayed on the same plot. The trend of increasing [Mn/Fe] with increasing [Zn/H], seen in the Milky Way stars, is clearly present in the absorber galaxies as well. Kendall's τ for the complete absorber sample (DLA + Sub-DLA) was determined to be τ = 0.724 with the probability of no correlation being 0.002. A Spearman rank correlation test gave the correlation coefficient ρ = 0.521 with the probability of no correlation of 0.006. Although the absorber sample shows a general correlation, the dispersion in the absorber data is larger compared to the stellar sample from Reddy, Lambert, & Prieto (2006). The fact that galaxies detected

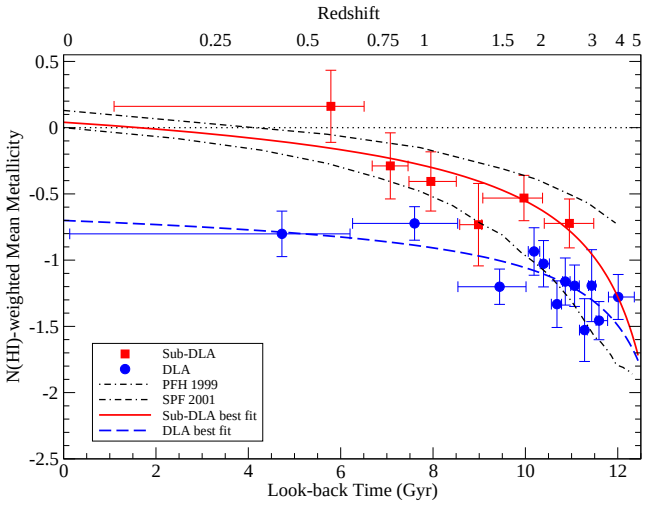

Figure 11. $N(\mathrm{H\,I})$-weighted mean metallicity vs. look-back time relation for 195 DLAs and 68 sub-DLAs with Zn or S measurements. Filled circles show 12 bins with 16 or 17 DLAs each. Squares denote 6 bins with 11 or 12 sub-DLAs each. Horizontal bars denote ranges in look-back times covered by each bin. Vertical errorbars denote 1 σ uncertainties. The bold solid and dashed curves show the best fits obtained from linear regression of the metallicity vs. redshift data for sub-DLAs and DLAs, respectively. The light dot-dashed and dot-double-dashed curves show, respectively, the mean metallicity in the models of Pei et al. (1999) and Somerville et al. (2001). Sub-DLAs appear to be more metal-rich and faster-evolving than DLAs, at all redshifts where both DLA and sub-DLA metallicity data exist ($z \lesssim 3$).

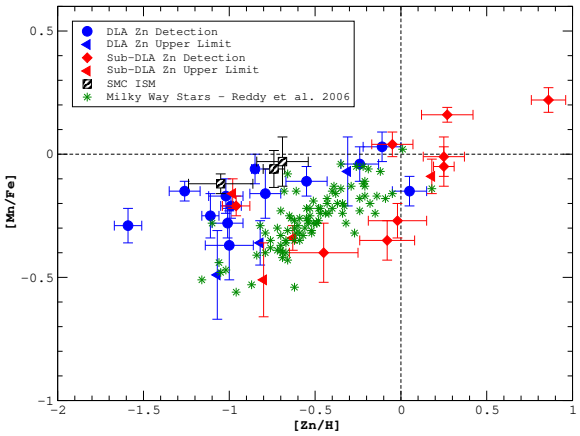

Figure 12. [Mn/Fe] vs. [Zn/H] for the sub-DLAs from this sample, as well as for sub-DLAs and DLAs from the literature. Milky Way stellar abundance data from Reddy, Lambert, & Prieto (2006) are shown overplotted. Also shown are the interstellar abundance data for SMC from Welty et al. (2001).

through absorption represent various morphological types is likely to cause this dispersion with additional contribution from differential depletion onto dust grains between Mn and Fe. Kendall's τ for the DLA sample alone was determined to be τ = 0.917 (with a probability of no correlation being 0.006), while τ = 0.872 for the sub-DLAs with a probability of obtaining this value by chance being 0.026. There seems to be evidence for different [Mn/Fe] versus [Zn/H] trends between DLAs and sub-DLAs. While the DLA measurements are similar to the interstellar abundance data from the SMC, the sub-DLA data bear resemblance with the Mn and Fe abundance pattern seen in the Galactic bulge stars (see e.g, McWilliam et al. 2003). The linear regression slopes for the [Mn/Fe] vs. [Zn/H] data, being 0.12 ± 0.04 and 0.27 ± 0.03 for DLAs and sub-DLAs, respectively, differ at $\sim 3\sigma$ level. However, larger samples are needed to confirm this difference. A difference in the [Mn/Fe] vs. [Zn/H] relations for DLAs and sub-DLAs may suggest a difference in the stellar populations in these two classes of absorbers.

5.5 Velocity Dispersion-Metallicity Relationship

Based on a sample of star-forming galaxies at z$\sim$0.1, Tremonti et al. (2004) found a correlation between stellar mass and gas-phase metallicity for these galaxies. Similar mass-metallicity relations have been suggested by Savaglio et al. (2005) for $0.4 < z < 1.0$ galaxies selected from the Gemini Deep Deep Survey and the Canada-France Redshift Survey and by Erb et al. (2006) for UV-selected star forming galaxies at $z \sim 2.3$. Nestor et al. (2003) and Turnshek et al. (2005) noticed a correlation between the Mg II λ 2796 equivalent width and the metallicity for strong Mg II absorbers at $1 \lesssim z \lesssim 2$. The possible existence of a mass metallicity relationship for DLA absorbers, assuming

Table 10. Velocity width values for the absorbers in this sample.

QSO	z_{abs}	[Zn/H]	Δv_{90} km s^{-1}	Selected transition line
Q1039-2719	2.139	-0.02 ± 0.17	70	Fe II λ 2374
Q1103-2645	1.839	<-0.82	81	Fe II λ 2600
Q1311-0120	1.762	>-0.04	152	Fe II λ 2374
Q1551+0908	2.320	<-0.95	32	Fe II λ 2344
Q2123-0050	2.058	$+0.25\pm0.12$	321	Fe II λ 2344

the velocity width of optically thin lines to be proportional to the mass, has recently been put into evidence (Péroux et al. 2003a; Ledoux et al. 2006). As the velocity width of the low-ionisation absorption lines potentially probes the depth of the underlying gravitational potential well of the DLA systems, this quantity can be used as a proxy for the stellar mass of these systems, which has been difficult to measure. Bouché et al. (2006), however, find an anti-correlation between the Mg II equivalent width and the estimated halo mass based upon an indirect mass indicator. Also, Zwaan et al. (2008) show that the velocity width and mass do not correlate well in local analogues of DLAs.

To investigate the velocity width-metallicity relation in sub-DLAs, we measured the velocity width values for the systems in our sample following the analysis of Wolfe & Prochaska (1998). The velocity width for a system was measured using an absorption profile (in velocity space) from a low-ion transition seen in the system. High-ionisation lines are not suitable for this analysis as their velocity widths are likely to be dominated by large scale thermal motions in the gas. The measurement method involved the conversion of the low-ion transition profile, $\mathrm{I}_{obs}(\mathrm{v})$, into the corresponding apparent optical depth profile, $\tau(\mathrm{v})_a$, through the following relation

$$\tau(\mathrm{v})_\mathrm{a} = \ln[\mathrm{I}_0(\mathrm{v})/\mathrm{I}_\mathrm{obs}(\mathrm{v})],$$

where $\mathrm{I}_0(\mathrm{v})$ represents the continuum level, and $\mathrm{I}_{obs}(\mathrm{v})$ is the observed intensity of the normalised transition profile in velocity space. The apparent optical depth was then integrated over the entire line profile to yield τ_{int}, the total optical depth within the

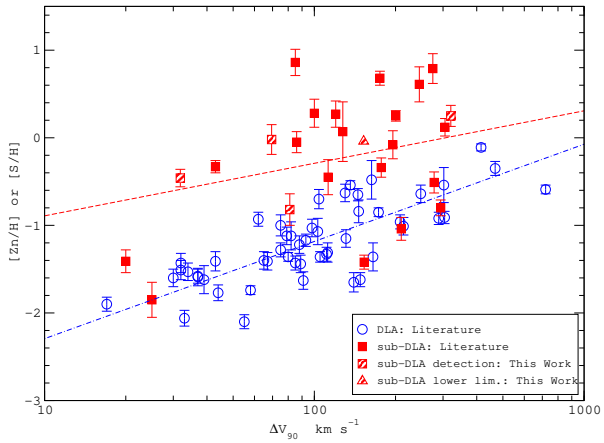

Figure 13. Velocity dispersion (ΔV_{90}) vs. Metallicity relations for sub-DLAs and DLAs. Linear regression fits to the sub-DLA and DLA data are shown as dashed and dashed-dotted lines respectively.

absorption profile. Finally, the velocity width was determined as $\Delta \mathrm{v}_{90} = [\mathrm{v}(95\%) - \mathrm{v}(5\%)]$, where $\mathrm{v}(95\%)$ and $\mathrm{v}(5\%)$ define the velocity range within which 90% of τ_{int} was contained.

In the case of very strong line profiles, the optical depth can not be measured accurately and the velocity width determined using such a line can be overestimated. On the other hand, velocity width measured from a very weak line becomes highly sensitive to the continuum noise and can be underestimated, as part of the absorbing gas can remain undetected. To select profiles which are neither strongly saturated nor too weak, we required the transitions profiles used to measure the velocity widths to satisfy $0.1 < \mathrm{I}_{min}/\mathrm{I}_c < 0.6$, where I_c is the continuum level intensity, and I_{min} is the intensity at the location of the strongest absorption in the line profile. After selecting a profile, we visually inspected the strongest low-ion transitions to ascertain the velocity range over which the selected profile should be integrated to determine $\Delta \mathrm{v}_{90}$. Table 10 lists the velocity width measurements from our systems along with the line profiles used.

In Figure 13 we plot the velocity dispersion versus metallicity based on Zn or S from our sample as well as for DLAs and sub-DLAs from the literature. Only systems for which Zn or S was detected were plotted. A correlation between velocity width and metallicity seems to exist for DLAs, while the sub-DLA data appear much less correlated. The sub-DLAs seem to be different from the DLAs also in terms of the mean metallicity. A linear regression fit for the sub-DLAs gives

$$[X/H] = (0.60 \pm 0.07) \log \Delta v_{90} - (1.49 \pm 0.15),$$

while a fit to the DLA data yields a slope of 1.11±0.03 and an intercept -3.40±0.06. The two slopes are different at $\sim 7\sigma$ level.

5.6 C II* Absorption and Cooling Rate

Most of the cooling in the Milky Way's interstellar medium takes place through the fine-structure line emission of [C II] λ158 μm. This line arises from the $^2P_{3/2}$ to $^2P_{1/2}$ transition in the ground state $2s^2\,2p$ term of C II. Following Pottasch, Wesselius, & van Duinen (1979), the rate of cooling per

Table 11. Cooling rate values for the absorbers in this sample

QSO	log $N_{H\ I}$ cm^{-2}	N_{CII^*} cm^{-2}	l_c ergs s^{-1} per H atom
Q1039-2719	19.55±0.15	$> 3.92 \times 10^{13}$	$> 3.33 \times 10^{-26}$
Q1103-2645	19.52±0.01	$> 8.53 \times 10^{12}$	$> 7.80 \times 10^{-27}$
Q1551+0908	19.70±0.05	$< 1.48 \times 10^{12}$	$< 8.93 \times 10^{-28}$
Q2123-0050	19.35±0.10	$> 6.60 \times 10^{13}$	$> 8.90 \times 10^{-26}$

H atom in gas detected in absorption can be expressed as:

$$l_c = \frac{N_{\mathrm{CII}^*} h\nu_{ul} A_{ul}}{N_{\mathrm{HI}}} \ \ \mathrm{ergs\ s^{-1}},$$

where N_{CII^*} is the column density of the C II ions in the $2P_{3/2}$ state, N_{HI} is the H I column density, while $h\nu_{ul}$ and A_{ul} are the energy of the $^2P_{3/2}$ to $^2P_{1/2}$ transition and coefficient for spontaneous photon decay, respectively. UV transitions of C II* λ1335.7 and Lyα λ1215.7 can be used to infer $\mathrm{N_{CII^*}}$ and $\mathrm{N_{HI}}$, respectively, for the determination of $\mathrm{l_c}$ in the interstellar medium detected in absorption.

Our data shows the presence of C II* λ1335.7 in the sub-DLAs toward Q1039-2719, Q1103-2645 and Q2123-0050. However, this line is partially blended with C IIλ1334 in Q1039-2719 and Q2123-0050 (see Figures 2 and 9, respectively) while for Q1103-2645, it is partially blended with a Lyα forest feature. As a result, only a lower limit on $\mathrm{N_{CII^*}}$ could be placed for each of these absorbers. However, the absorption profile structures of these systems suggest that the true $\mathrm{N_{CII^*}}$ values are unlikely to be much higher than the corresponding lower limits. For the sub-DLA toward Q1551+0908, C II* λ1335.7 was not detected and we placed a 3σ upper limit on $\mathrm{N_{CII^*}}$ based on the S/N near the line. Poor S/N in the region of the transition did not allow us an estimate of C II* abundance in the sub-DLA toward Q1311-0120. Table 11 lists the $\mathrm{N_{CII^*}}$ and the corresponding $\mathrm{l_c}$ values for the sub-DLAs in this sample.

The cooling rate versus H I column density data for these sub-DLAs are plotted in Figure 14, along with the corresponding measurements for DLAs from Wolfe et al. (2003) and for interstellar clouds in the Milky Way adopted from Lehner et al. (2004). The ISM measurements are shown separately for low, low+intermediate, intermediate, and high-velocity clouds in the Milky Way. Although our measurements could only provide limits on the sub-DLA cooling rates, it can immediately be inferred from Fig. 14 that, with the exception of the absorber toward Q1551+0908, these systems show higher cooling rates compared to the QSO DLAs and similar values to those seen in the Milky Way interstellar clouds. We also note, assuming the true cooling rates lie close to the observed lower limits, that the sub-DLA showing the highest cooling rate is also the most metal-rich absorber in our sample while the system with the least metallicity happens to show the lowest $\mathrm{l_c}$ value. This, combined with the measurements on the other absorbers from our sample, points to the possibility that the cooling rate in sub-DLAs may increase with metallicity. However, a detailed investigation of the metallicity dependence of cooling rate in sub-DLAs warrants a much larger sample with precise column density determinations.

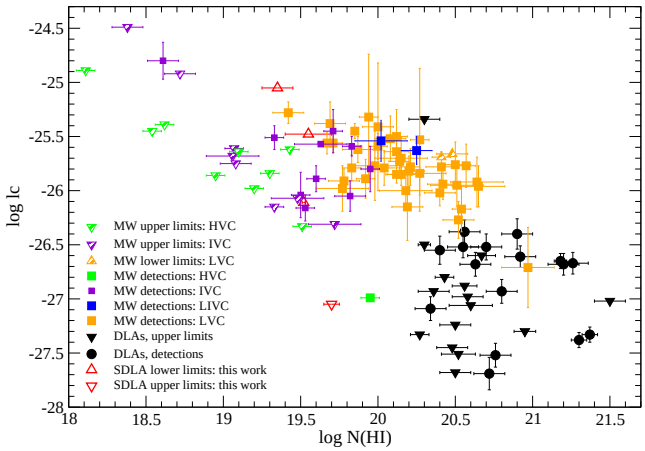

Figure 14. Cooling rate estimated from C II* absorption plotted vs. H I column density. The open red triangles represent the sub-DLAs from our sample. The filled black circles and triangles denote the sample of QSO DLAs in Wolfe et al. (2003). The filled squares and striped triangles represent the measurements for low, intermediate, low+intermediate, and high-velocity interstellar H I clouds in the Milky Way compiled in Lehner et al. (2004).

6 CONCLUSIONS

In this paper, we have presented high-resolution absorption spectra of 5 sub-DLAs at $1.7 < z_{abs} < 2.4$. Although, to date the DLA systems have been the preferred tracer of metallicity at high redshift, most of the absorbers observed to have solar or higher metallicity have been sub-DLAs (e.g., Pettini et al. 2000; Khare et al. 2004; Péroux et al. 2006a; Prochaska et al. 2006; Meiring et al. 2007, 2008, 2009). With the sub-DLA sample presented in this paper, we have found a system with $[\mathrm{Zn/H}] > -0.06$ dex at $z_{abs} = 1.76$ and two systems with $[\mathrm{Zn/H}] = +0.25$ dex and $[\mathrm{Zn/H}] = -0.02$ dex (+0.84 dex and +0.48 dex, respectively, after ionisation correction) at $z_{abs} > 2$. These two systems are the most metal-rich sub-DLAs known so far at $z_{abs} \gtrsim 2$. These observations suggest that metal-rich sub-DLAs appear at high redshift as well. Combining the data presented in this paper with other sub-DLA and DLA data from the literature, we have also reported the most complete existing determination of the $\mathrm{N_{H\ I}}$-weighted mean metallicity vs. redshift relation for sub-DLAs and DLAs. The results show that the trend of higher mean metallicity in sub-DLAs compared to DLAs, observed previously at $z < 1.5$, continues to exist at least upto $z \lesssim 3$. We also find that while metallicity evolution in DLAs does not resemble the expected mean trend for chemical enrichment in galaxies, the sub-DLA data are consistent with the chemical evolution models at all redshifts probed so far. It is possible that most of the DLA host galaxies have not undergone much star formation even by the current epoch but the majority of the sub-DLAs trace massive star forming galaxies. To gain additional insights into the nature of DLAs and sub-DLAs, we compared their [Mn/Fe] vs. metallicity trends and the results suggest a difference in the stellar populations for the galaxies traced by these two classes of QSO absorbers. We also compare the velocity dispertion vs. metallicity trends for these absorbers and find that, while metallicity correlates with velocity dispertion in DLAs, the sub-DLA data show a lower degree of correlation. Finally, we estimated cooling rates for the sub-DLAs in our sample using the C II* λ1335.7 line, and compared them with the DLA data available in the literature. The observed lower limits suggest that metal rich QSO sub-DLAs can show higher cooling rates than those seen in the QSO DLAs.

ACKNOWLEDGMENTS

We are grateful to an anonymous referee for comments that have helped to improve this paper. We also thank the helpful staff of Las Campanas Observatory for their assistance during the observing runs. D. Som and V. P. Kulkarni gratefully acknowledge support from the U.S. National Science Foundation grants AST-0908890 and AST-1108830 (PI Kulkarni).

REFERENCES

Akerman C. J., Ellison S. L., Pettini M., Steidel C. C., 2005, A&A, 440, 499
Battisti A. J., Meiring J. D., Tripp T. M., Prochaska J. X., Werk J. K., Jenkins E. B., Lehner N., Tumlinson J., Thom C., 2012, ApJ, 744, 93
Bernstein R., Schectman S. A., Gunnels S., Mochnacki S., Athey A., 2003 SPIE, 4841, 1694
Boissé P., Le Brun V., Bergeron J., Deharveng J. M., 1998, A&A, 333, 841
Bouche N., Murphy M. T., Pèroux C., Csabai I., Wild V., 2006, MNRAS, 371, 495
Centurión M., Molaro P., Vladilo G., Péroux C., Levshakov S. A., D'Odorico V., 2003, A&A, 403, 55
Chen H-W., Lanzetta K. M., 2003, ApJ, 597, 706
Davé R., Oppenheimer B. D., 2007, MNRAS, 374, 427
de la Varga A., Reimers D., Tytler D., Barlow T., Burles S., 2000, A&A, 363, 69
Dessauges-Zavadsky M., Péroux C., Kim T.-S., D'Odorico S., McMahon R. G., 2003, MNRAS, 345, 447
Dessauges-Zavadsky M., Ellison S. L., Murphy M. T., 2009, MNRAS, 396, 61
Ellison S. L., Lopez S., 2001, A&A, 380, 117
Erb D. K., Shapely A. E., Pettini M., Steidel C. C., Reddy N. A., Adelberger K. L., 2006, ApJ, 644, 813
Fang T., Marshall, H. L., Lee J. C., Davis D. S., Canizares C. R., 2002, ApJ, 527, 127
Ferland G. J., Porter R. L., van Hoof P. A. M., Williams R. J. R., Abel N. P., Lykins M. L., Shaw G., Henney W. J., Stancil P. C., 2013, RMxAA, 49, 137
Fynbo J. P. U., Prochaska J. X., Sommer-Larsen J., Dessauges-Zavadsky, M., Møller P., 2008, ApJ, 683, 321
Fynbo J. P. U., Ledoux C., Noterdaeme P., Christensen L., Møller P., Durgapal A. K., et al., 2011, MNRAS, 413, 2481
Ge J., Bechtold J., Kulkarni V. P., 2001, ApJ, 547, L1
Gharanfoli S., Kulkarni V. P., Chun M. R., Takamiya M., 2007, ApJ, 133, 130
Gratton R. G., Caretta E., Claudi R., Lucatello S., Barbieri M., 2004, A&A, 404, 187
Haardt F., Madau P., 1996, ApJ, 461, 20
Howk J.C., Sembach K.R., 1999, ApJ, 523, L141
Kaplan K. F., Prochaska J. X., Herbert-Fort S. Ellison S. L., Dessauges-Zavadsky M., 2010, PASP, 122, 619
Khare P., Kulkarni V. P., Lauroesch J. T., York D. G, Crotts P. S., Nakamura O., 2004, ApJ, 616, 86
Kulkarni V. P., Bechtold J., Ge J., 1999, in Proc. ESO Workshop,

Chemical Evolution from Zero to High Redshifts, ed. M. Rosa & J. Walsh (Berlin: Springer), 275
Kulkarni V. P., Fall S. M., 2002, ApJ, 580, 732
Kulkarni V. P., Fall S. M., Lauroesch J. T., York D. G, Welty D. E, Khare P., Truran J. W., 2005, ApJ, 618, 68
Kulkarni V. P., Khare P., Pèroux C., York D. G., Lauroesch J. T., Meiring J. D., 2007, ApJ, 661, 88
Kulkarni V. P., Khare P., Som D., Meiring J. D., York D. G., Pèroux C., Lauroesch J. T., 2010, NewA, 15, 735
Ledoux C. Petitjean P., Møller P., Fynbo J., Srianand R., 2006, A&A, 457, 71
Lehner N., Wakker B. P., Savage B. D., 2004, ApJ, 615, 767
Lodders K., 2003, ApJ, 591, 1220
Lopez S., Reimers D., Rauch M., Sargent W. L. W., Smette A., 1999, ApJ, 513, 598
Lopez S., Reimers D., D'Odorico S., Prochaska J. X., 2002, A&A, 385, 778
Lopez S., Ellison S. L., 2003, A&A, 403, 573
Lu L., Savage B. D., Tripp T. M., Meyer D. M., 1995, ApJ, 447, 597
Lu L., Sargent W. L. W., Barlow T. A., Churchill C. W., Vogt S. S., 1996, ApJS, 107, 475
Madau P., Haardt F., Rees M.J., 1999, ApJ, 514, 648
Maiolino R., Nagao T., Grazian A., Cocchia F. et al., 2008, A&A, 488, 463
McWilliam A., Rich R. M., Smecker-Hane T. A., 2003, ApJ, 592, L21
Meiring J. D., Kulkarni V. P., Khare P., Bechtold J., York D. G., Cui J., Lauroesch J. T., Crotts A. P. S., Nakamura O., 2006, MNRAS,370, 43
Meiring J. D., Lauroesch J. T, Kulkarni V. P., Péroux C., Khare P., York D. G., Crotts A. P. S., 2007, MNRAS,376, 557
Meiring J. D., Kulkarni V. P., Lauroesch J. T., Péroux C., Khare P., York D. G., Crotts A. P. S., 2008, MNRAS,384, 1015
Meiring J. D., Kulkarni V. P., Lauroesch J. T., Péroux C., Khare P., York D.G., 2009, MNRAS,393, 1513
Meyer D. M., York D. G., 1992, ApJ, 399, L121
Meyer D. M., Lanzetta K. M., Wolfe A. M., 1995, ApJ, 451, L13
Molaro P., Bonifacio P., Centurión M., D2̃019Odorico S., Vladilo G., Santin P., Di Marcantonio P., 2000, ApJ, 541, 54
Morton D. C., 2003, ApJS, 149, 205
Nestor D. B., Rao S. M., Turnshek D. A., Vanden Berk D., 2003, ApJ, 595, L5
Nestor D. B., Pettini M., Hewett P. C., Rao S., Wild V., 2008, MNRAS, 390, 1670
Nissen P. E., Chen Y. Q., Schuster W. J., Zhao G., 2000, A&A, 353, 722
Nissen P. E, Chen Y. Q., Asplund M., Pettini M., 2004, A&A, 415, 993
Noterdaeme P., Ledoux C., Petitjean P., Srianand R., 2008, A&A, 481, 327
Noterdaeme P., Petitjean P., Ledoux C., Srianand R., 2009, A&A, 505, 1087
Pei Y. C., Fall S. M., Hauser M. G., 1999, ApJ, 522, 604
Péroux C., Storrie-Lombardi L., McMahon R., Irwin M., Hook I., 2001, AJ, 121, 1799
Péroux C., Petitjean P., Aracil B., Srianand R., 2002, NewA, 7, 577
Péroux C., Dessauges-Zavadsky M., D'Orico S., Kim T. S., McMahon R., 2003, MNRAS, 345, 480
Péroux C., Kulkarni, V. P., Meiring J., Ferlet R., Khare P., Lauroesch J. T., Vladilo G., York D. G, 2006, A&A, 450, 53
Péroux C., Meiring J., Kulkarni V. P., Ferlet R., Khare P., Lauroesch J. T., Vladilo G., York D. G., 2006, MNRAS, 372, 369
Péroux C., Meiring J. D., Kulkarni V. P., Khare P., Lauroesch J. T., Vladilo G., York D. G., 2008, MNRAS, 386, 2209
Petitjean P., Webb J. K., Rauch M., Carswell R. F., Lanzetta K., 1993, MNRAS, 262, 499
Petitjean P., Srianand R., Ledoux C., 2000, A&A, 364, 26
Pettini M., Smith L. J., Hunstead R. W., King D. L., 1994, ApJ, 426, 79
Pettini M., King D. L., Smith L. J., Hunstead R. W., 1997, ApJ, 478, 536
Pettini M., Ellison S. L., Steidel C. C., Bowen D. V., 1999, ApJ, 510, 576
Pettini M., Ellison S. L., Steidel C. C., Shapley A. E., Bowen, D.V., 2000, ApJ, 532, 65
Pettini M., 2004, in Proc. XIII Canary Islands Winter School of Astrophysics, Cosmochemistry: The Melting Pot of Elements, ed. C. Esteban, R. J. Garcí López, A. Herrero & F. Sánchez, 257
Pottasch S. R., Wesselius P. R., & van Duinen R. J., 1979, A&A, 77, 189
Prochaska J. X., Wolfe A. M., 1998, ApJ, 507, 113
Prochaska J. X., Wolfe A. M., 1999, ApJS, 121, 369
Prochaska J. X., Gawiser E., Wolfe A. M., 2001, ApJ, 552, 99
Prochaska J. X., Wolfe A. M., 2002, ApJ, 566, 68
Prochaska J.X., Howk J.C., O'Meara J.M., Tytler D., Wolfe A.M., Kirkman D., Lubin D., Suzuki N., 2002, ApJ, 571, 693
Prochaska J. X., Castro S., Djorgovski S. G., 2003, ApJS, 148, 317
Prochaska J. X., Gawiser E., Wolfe A. M., Cooke J., Gelino D., 2003, ApJS, 147, 227
Prochaska J. X., O'Meara J. M., Herbert-Fort S., Burles S., Prochter G. E., Bernstein R. A., 2006, ApJ, 648, L97
Rafelski M., Wolfe A. M., Prochaska J. X., Neeleman M., Mendez A. J., 2012, ApJ, 755, 89
Rao S. M., Prochaska J. X., Howk C., Wolfe A. M., 2005, AJ, 129, 9
Reddy B. E., Lambert D. L., Prieto C. A., 2006, MNRAS, 367, 1329
Savage B. D., Sembach K. R., 1996, ApJ, 379, 245
Savaglio S., Glazebrook K., Le Borgne D., Juneau S., Abraham R. G., Chen H.-W., Crampton D., McCarthy P. J., Carlberg R. G., Marzke R. O., Roth K., Jrgensen I., Murowinski R., 2005, ApJ, 635, 260
Savaglio S., Glazebrook K., Le Borgne D., 2009, ApJ, 691, 182
Savaglio S., Rau A., Greiner J., Krühler T., McBreen S., Hartmann D. H., et al., 2012, MNRAS, 420, 627
Schaye J., 2006, ApJ, 643, 59
Simcoe R. A, Sargent W. L. W, Rauch M., 2002, ApJ, 578, 737
Somerville R. S., Primack J. R., Faber S. M., 2001, MNRAS, 320, 504
Srianand R., Petitjean P., 2001, A&A, 373, 816
Tremonti C. A., Heckman T. M., Kauffmann G. et al. 2004, ApJ, 613, 898
Turnshek D. A. et al. 2005, in Proc. IAU Colloquium No. 199: Probing Galaxies through Quasar Absorption Lines, ed. P. R. Williams, C. Shu, & B. Ménard, 104
Vidal-Madjar A., Laurent C., Bonnet R. M., York, D. G, 1977, 211, 91
Vladilo G., Centurión M., Bonifacio P., Howk C., 2001, ApJ, 557, 1007
Welty D. E., Hobbs L. M., York D.G., 1991, ApJS, 75, 425
Welty D. E., Lauroesch J. T., Blades C., Hobbs L. M., York D. G.,

2001, ApJ, 554, 75
Wolfe A. M., Lanzetta K. M., Foltz C. B., Chaffee F. H., 1995, ApJ, 454, 698
Wolfe A. M., & Prochaska, J. X., 1998, ApJ, 494, L15
Wolfe A. M., Prochaska J. X., Gawiser, E., 2003, ApJ, 593, 215
York D. G., Khare P., Vanden Berk D., Kulkarni V. P., Crotts A. P. S., Lauroesch J. T., Richards G. T., et al., 2006, MNRAS, 367, 945
Zwaan M., Walter F., Ryan-Weber E., Brinks E., de Blok W. J. G., Kennicutt R. C., 2008, AJ, 136, 2886

This paper has been typeset from a TEX/ LATEX file prepared by the author.